

# Time-series single-cell transcriptomic profiling of luteal-phase endometrium uncovers dynamic characteristics and its dysregulation in recurrent implantation failures

Received: 28 December 2023

Accepted: 9 December 2024

Published online: 02 January 2025


 Check for updates

Dandan Cao<sup>1,10</sup>, Yijun Liu<sup>2,3,10</sup>, Yanfei Cheng<sup>1,10</sup>, Jue Wang<sup>1</sup>, Bolun Zhang<sup>1,4</sup>, Yanhui Zhai<sup>1</sup>, Kongfu Zhu<sup>1</sup>, Ye Liu<sup>1</sup>, Ye Shang<sup>1</sup>, Xiao Xiao<sup>5</sup>, Yi Chang<sup>3</sup>, Yin Lau Lee<sup>1,6,7</sup>, William Shu Biu Yeung<sup>1,6,7</sup> , Yuanhua Huang<sup>2,7,8</sup>  & Yuanqing Yao<sup>1,9</sup> 

Understanding human endometrial dynamics in the establishment of endometrial receptivity remains a challenge, which limits early diagnosis and treatment of endometrial-factor infertility. Here, we decode the endometrial dynamics of fertile women across the window of implantation and characterize the endometrial deficiency in women with recurrent implantation failure. A computational model capable of both temporal prediction and pattern discovery is used to analyze single-cell transcriptomic data from over 220,000 endometrial cells. The time-series atlas highlights a two-stage stromal decidualization process and a gradual transitional process of the luminal epithelial cells across the window of implantation. In addition, a time-varying gene set regulating epithelium receptivity is identified, based on which the recurrent implantation failure endometria are stratified into two classes of deficiencies. Further investigation uncovers a hyper-inflammatory microenvironment for the dysfunctional endometrial epithelial cells of recurrent implantation failure. The holistic characterization of the physiological and pathophysiological window of implantation and a computational tool trained on this temporal atlas provide a platform for future therapeutic developments.

The human endometrium is a highly dynamic tissue that undergoes cyclical regeneration, differentiation, and shedding under the primary control of ovarian follicle-derived estrogen and corpus luteum-derived progesterone. The monthly menstrual cycle is divided into menstrual, proliferative, periovulatory, and secretory phases according to the endometrial morphology<sup>1</sup>. In the secretory phase, the human endometrium differentiates into a state receptive to embryo implantation<sup>2</sup>.

The receptive interval known as the window of implantation (WOI) is short and commences on day 7 after luteinizing hormone surge (LH + 7)<sup>3</sup>. In the WOI, the endometrial stromal, epithelial, endothelial, and immune cells coordinately create a receptive microenvironment in the endometrium, and a synchronized embryo-endometrium crosstalk at this stage is a prerequisite for a successful implantation and subsequent pregnancy<sup>4</sup>. The importance of blastocyst-endometrium

A full list of affiliations appears at the end of the paper.  e-mail: [wsbyeung@hku.hk](mailto:wsbyeung@hku.hk); [yuanhua@hku.hk](mailto:yuanhua@hku.hk); [yaoyq\\_hkusz@126.com](mailto:yaoyq_hkusz@126.com)

crosstalk on implantation is well documented. Intrauterine infusion of spent culture medium of implanted human embryos enhances expression of metabolic and implantation related genes, whereas those from poor quality embryos induces stress response of the mouse endometrium<sup>5</sup>. The human endometrial stromal cells are biosensors of the embryo quality<sup>6</sup> and respond to embryo-derived hsa-miR-320a by modifying their migratory capacity towards high quality blastocysts<sup>7</sup> and to a serine protease from poor quality embryos by reducing the production of implantation related factors<sup>8</sup>. Secretion of the poor-quality embryos also abolished the killing of senescent endometrial stromal cells by uterine natural killer cells<sup>9</sup>. The biosensing function of decidualized endometrial stromal cells has been proposed as one of the implantation checkpoints, and its impairment may account for the maternal age-independent stepwise increase in miscarriage rates after each pregnancy loss<sup>10</sup>. On the other hand, embryo attachment onto endometrial epithelial cells promotes differentiation of syncytiotrophoblast from<sup>11</sup> and expression of adhesion molecules on<sup>12</sup> the trophoblast of human blastocysts. Endometrium-derived exosomal microRNA let-7 induce diapause of mouse blastocysts and inhibit trophoblast differentiation in a human embryo surrogate model<sup>13</sup>. A compromised crosstalk between the endometrium and embryos causes fertility problems such as recurrent implantation failure (RIF)<sup>14</sup>.

One commonly used definition of RIF is the failure to achieve a clinical pregnancy after the transfer of at least four good-quality cleavage embryos in a minimum of three cycles in a woman <40 years of age<sup>15</sup>. RIF is a major obstacle in assisted reproduction technology treatment and causes psychological pain to the patients. Both embryonic and endometrial factors contribute to RIF pathogenesis. The effect of embryonic factors has recently been reduced using advanced embryo selection techniques such as time-lapse morphokinetic embryo selection and pre-implantation genetic testing for aneuploidy (PGT-A). However, the treatment methods for endometrial factor infertility remain rudimentary<sup>16</sup>. Although bulk transcriptomic studies have identified displaced WOI and in-phase pathological gene signatures of RIF<sup>17</sup>, they fail to pinpoint the cellular-specific features in the RIF endometrium.

Recent application of single-cell transcriptome sequencing technology to endometrial studies greatly improves our temporal and spatial insights into the cell type composition, molecular profiles and dynamics, regulatory mechanism of epithelial subtype differentiation in healthy human endometrium<sup>18,19</sup>, as well as dysregulated cellular and molecular programs in disturbed conditions such as endometriosis<sup>20,21</sup>, thin endometrium<sup>22</sup>, and Asherman syndrome<sup>23</sup>. Previous single-cell studies on WOI and RIF either had a limited sample size or collected endometrial biopsy without precise menstrual cycle dating, which may cause misinterpretations<sup>18,24,25</sup>. Daily serum LH measurement could provide precise timing of the WOI, and knowledge of normal dynamic changes in endometrial gene expression during the WOI could serve as a reference for a comprehensive characterization of endometrial disorders.

In this study, we used single-cell transcriptomic sequencing and computational analysis to interrogate the cellular states, molecular dynamics, and interactions of human endometrial cells across WOI in fertile women. We also investigated the endometrial factors at WOI in women with RIF. We developed an algorithm, StemVAE to model the time-series single-cell data of the endometrium (LH + 3 to LH + 11) to elucidate its transcriptomic dynamics in descriptive and predictive manners. We uncovered a clear-cut two-stage decidualization process for the stromal cells and a gradual transition process for the epithelial cells across the WOI. We also defined a set of epithelial receptivity genes and identified stromal and epithelial regulators shaping the immune microenvironment. Finally, displaced WOI and dysregulated epithelium in a hyper-inflammatory microenvironment were identified in the RIF endometria. The findings strengthen the knowledge of WOI from both physiological and pathophysiological views and provide insights into the improvement of human fertility.

## Results

### High-resolution single-cell landscape of human endometrium across WOI

To generate a high-resolution cellular map of human endometrium across WOI and to characterize the endometrial cellular profiles affecting embryo implantation, endometrial aspirates from fertile women and women with RIF were subjected to droplet-based scRNA-seq (see Methods, Fig. 1a). In total, 28 endometrial biopsies spanning 5 time points around the WOI (LH + 3, LH + 5, LH + 7, LH + 9, LH + 11) were included (Supplementary Data 1). The time-point LH + 7 consisted of two types of donors, namely fertile women ( $n = 6$ ), and women with RIF ( $n = 10$ ). The other time points contained samples only from fertile women ( $n = 3$  for each time point). All the recruited women had regular menstrual cycles. Dates of the menstrual cycle were relative to LH surge as determined by serial blood tests for LH (see Methods). The collected endometrial biopsies were enzymatically dispersed, and single cells were captured using a 10X Chromium system (see Methods).

In total, 220,848 cells with a median of 8481 unique transcripts and 2983 genes per cell (Supplementary Fig. 1a–d) were retained after doublet removal and filter of low-quality cells (see Methods). Eight segregated groups of cells were determined after batch correction and were manually annotated as unciliated (37,152, 16.8%) and ciliated epithelial cells (4326, 1.9%), stromal cells (79,183, 35.8%), endothelial cells (1318, 0.6%), natural killer (NK)/T cells (85,060, 38.5%), myeloid cells (8313, 3.8%), B cells (4057, 1.8%) and mast cells (1439, 0.6%) with expression of corresponding well-recognized marker genes (Fig. 1b, c, Supplementary Fig. 2a). Collectively, the NK/T, stromal and epithelial cells were the most abundant cell types, consistent with previous findings in human endometrial tissues<sup>18,19</sup>. There were large inter-individual variations in the cellular composition of the fertile individuals across the WOI (Supplementary Fig. 2a, b), in line with a previous single-cell study on healthy endometrium<sup>20</sup>. Deconvolution of published bulk RNA-seq data of human endometrium across the WOI also showed large variations in the cellular composition of major cell types among endometrial samples (Supplementary Fig. 2c). As we strictly controlled sample processing to minimize technical variation (see Methods), the inter-individual cellular differences among samples were likely due to genuine tissue variation. By considering the large variation which usually requires large sample size to achieve the power, we didn't perform cell type composition comparison in this study to get biological conclusions with such a limited sample size from a statistical view.

To delineate endometrial cellular landscape across WOI in high resolution, we performed clustering analysis within epithelial, stromal, NK/T, and myeloid cells. This analysis identified 8 epithelial cell subpopulations, 5 stromal cell subpopulations, 11 NK/T cell subpopulation and 10 myeloid cells subpopulations (Fig. 1b, Supplementary Fig. 1e–h), highlighting the complex cellular architecture of human endometrium. Inter-individual variations in the composition of the subpopulations were also observed (Supplementary Fig. 2d–g).

Based on UMAP visualization of transcriptomic dimensional reduction results, distinct luminal, glandular, unciliated secretory (high-PAEP expressing) and proliferative (cycling) epithelial subpopulations were identified (Fig. 1b, Supplementary Fig. 1e). Interestingly, the luminal cell population exhibited both luminal and glandular characteristics by expressing corresponding marker genes (luminal: *LGR4*, *FGFR2*, *ERBB4*; glandular: *MMP26*, *SPPI1*, *MUC16*). These cells were localized to the surface layer and the glandular area of the endometrium (Supplementary Fig. 1e, Supplementary Fig. 3a) by utilizing a public spatial transcriptomic dataset of secretory human endometrium<sup>19</sup>. To dissect the heterogeneity in the luminal cell subpopulation, we determined cell clusters of the subpopulation at different resolutions and constructed the cell cluster tree. Within the luminal group, subclusters were in the same tree instead of clustering

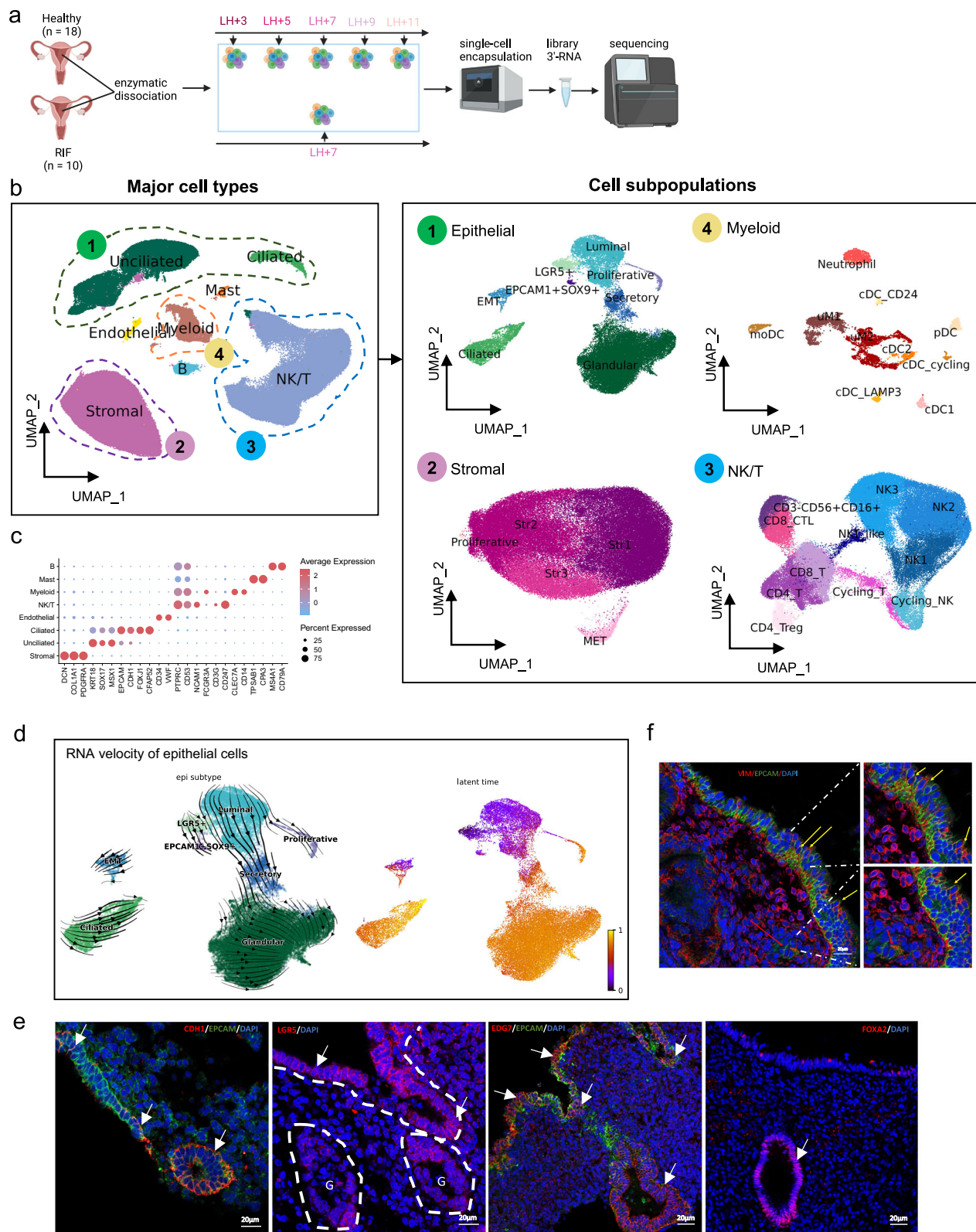


**Fig. 1 | Cellular landscape of human endometrium across the window of implantation.** **a** Schematic summary of the experimental design. Endometrial cells from fertile control and RIF were processed by single-cell 3' transcriptomic sequencing. Created in BioRender. Gong (2024) <https://BioRender.com/c12o660>. **b** UMAP plots of a total of 220,248 cells and epithelial, stromal, NK/T, and myeloid subsets color-coded by major cell types (left) and subpopulations (right), respectively. **c** The expression of marker genes for the major cell types. **d** The RNA velocity

trajectory (left) and latent time (right) for epithelial cell subpopulations. **e** Immunostaining of luminal marker genes (CDH1, LGR5, EDG7) and glandular marker gene (FOXA2) in endometrium of proliferative phase (n = 3). G: gland. **f** Immunostaining of epithelial cell marker EPCAM and stromal cell marker VIM in LH + 5 endometrial tissue (n = 1). Results for other time points could be found in Supplementary Fig. 5 (n = 4 in total). Source data are provided as a Source Data file.



with the secretory or glandular subclusters supporting their distinct identity (Supplementary Fig. 3b, c). We used reported luminal and glandular cell markers<sup>18,19,26</sup> for expression pattern analysis (Supplementary Fig. 3d). Spatially, the most luminal cell-like clusters (clusters 10, 22, 30 with high expression of *LIFR* and *LPAR3*) were localized to both the luminal surface and the glandular areas (Supplementary Fig. 3a–d). Interestingly, the luminal subpopulation exhibited a low latent time indicating relatively high differentiation potential (Fig. 1d). In addition, the vector stream of RNA velocity trajectory showed that the cells could differentiate toward glandular cells (Fig. 1d). Consistently, both uterine luminal epithelium and newly formed glands in proliferative phase endometrium expressed immuno-reactivities of luminal epithelial cell markers *LGR5* and *EDG7* (Fig. 1e). The expression of *LGR5* and *EDG7* in both epithelial cells was also observed in secretory endometrium (Supplementary Fig. 4). Therefore, we proposed that the identified luminal population represented a group of luminal cells which not only lined the uterine cavity but also extended to newly formed glands. Similar findings were also observed for the epithelial cell marker *CDH1*, but the expression of glandular-specific marker *FOXA2* was only detected in the glands (Fig. 1e) supporting our proposal.

Among the endometrial cells, a group of rare epithelial cells undergoing epithelial-mesenchymal transition (EMT) and another group of rare stromal cells undergoing mesenchymal-epithelial transition (MET) were observed (Fig. 1b, Supplementary Fig. 1e). They simultaneously expressed epithelial cell marker genes such as *KRT8*, *ALCAM*, and mesenchymal cell marker genes including *CDH11*, *COL1A1*, *COL3A1*, together with EMT/MET process regulators *TWIST2*, *ZEB1*, *ZEB2*, *SNAI2*, *EHF* and *PAX2* (Fig. 1b, Supplementary Fig. 1e). Potential EMT/MET cells co-expressing epithelial cell marker *EPCAM* and stromal cell marker *VIM* were also found through immunostaining (Fig. 1f) but with patient variability (Supplementary Fig. 5) which required future extensive study. The ability of our dataset to detect rare cells was reinforced by the identification of *EPCAM*<sup>+</sup>*SOX9*<sup>+</sup> progenitor cells which highly expressed *MUC5B* (Supplementary Fig. 1e), an endometrial epithelial progenitor marker<sup>20</sup>. A distinct *LGR5*<sup>+</sup> epithelial cell cluster was also revealed. *LGR5* is both a progenitor and a luminal marker in endometrium<sup>18,27</sup>. Interestingly, the stem cell regulator *FGFR2*<sup>28</sup> was highly expressed in this cluster suggestive of its stem/progenitor identity (Supplementary Fig. 1e). RNA velocity analysis suggested that the *LGR5*<sup>+</sup> cluster should be a progenitor cluster with lowest pseudo time (highest differentiation potential) when compared to other epithelial cells (Fig. 1d). Utilizing a public endometrial spatial transcriptomic dataset<sup>19</sup>, the *LGR5*<sup>+</sup> and the *EPCAM*<sup>+</sup>*SOX9*<sup>+</sup> cells were mainly located at the luminal surface and the basalis layer, respectively (Supplementary Fig. 3a). It is speculated that they represent two different populations of stem cells residing in the endometrium collectively responsible for endometrial regeneration and homeostasis<sup>27,29</sup>.

### A newly developed VAE model reveals time-variant and time-invariant endometrial cells

To decipher the temporal dynamics across WOI, we first identified potential time-associated genes using variancePartition<sup>30</sup> by considering the sampling time as a continuous variable (Methods). Interestingly, for the four major cell types (epithelial, stromal, NK/T, myeloid), the number of genes with at least 10% of the gene-level expression variance that could be explained by time in the epithelial (675 genes) and stromal cells (251 genes) differed significantly from that of the immune cells (NK/T: 2 genes, Myeloid: 5 genes), indicating their time-variant and time-invariant hormonal responses, respectively across the WOI (Supplementary Fig. 6a). Through inspection of well-known WOI-related genes in the epithelial cells and the stromal cells, we found temporal changes in endometrial activity across the WOI. For instance, there was a decreasing expression trend of hormone receptors *PGR* and *ESR1* in the epithelial cells (Supplementary Fig. 6b), but a

persistent expression pattern in the stromal cells (Supplementary Fig. 6c), as well as an increasing trend of *GPX3*, *DPP4* and *CXCL14*, which were used to establish the secretory endometrial dating method EndoTime<sup>31</sup> from LH + 3 to LH + 11 in the epithelial cells (Supplementary Fig. 6b, c).

As single cells from one time-point/sample represent a mixture of states, continuous time reconstruction should improve the investigation of the temporal dynamics. Existing unsupervised pseudotime computational techniques rarely infer time series-specific transcriptomic changes, and such methods therefore are suboptimal to generate individual cell orderings in this study. Here we developed StemVAE, a single-cell temporal inference model that leveraged a variational autoencoder with input of luteal time labels (LH+n) (Fig. 2a). Briefly, this approach is structured with one encoder on the observed cell-by-gene expression data with time labels and two decoders for reconstruction of cell-by-gene expression and luteal time of each cell, thereby establishing an order for the cells (Methods, Supplementary Note). StemVAE is highly flexible and capable of both temporal prediction and pattern discovery.

By applying StemVAE to the 130,094 cells from 18 fertile donors covering the WOI, the predicted cell orderings highly corresponded to the input time labels in overall cell populations or specifically to epithelial cells and stromal cells (Fig. 2b, Supplementary Fig. 7a). The predicted time distribution domain mostly remained within the same interval when StemVAE was built solely on the epithelial cells or the stromal cells (Supplementary Fig. 7b). Meanwhile, the orderings within each time-point showed major in-frame domain distribution together with preceding or lagging cells in the adjacent frames. The result was consistent with the idea that bulk assessments of cells at specific time points overlook for the heterogeneity and differential kinetics of responses exhibited by single cells. Based on the predictions, we quantified the time association across the WOI for each major cell type as well as their subpopulations by calculating the Spearman's rank correlation coefficient between sampling and predicted time. The results supported our speculation that the dynamic changes of the unciliated epithelial cells and the stromal cells were highly correlated with the time while that of the immune subsets as well as ciliated epithelial cells and endothelial cells showed moderate (around 0.5) or low (less than 0.5) time-association irrespective of the gene sets (HVGs or time-associated genes identified by variancePartition) that StemVAE was built on (Fig. 2c, Supplementary Fig. 8a).

To check the dynamics across WOI, we first identified genes that varied coherently along the predicted orders for each cell subset using mutual information (MI) calculation as previously reported in another endometrial study<sup>18</sup>. The MI score distribution of genes in different subsets consistently showed the time-variant characteristics of the epithelial cells and the stromal cells and the time-invariant properties of the immune cells (Supplementary Fig. 9) echoing the results from the variancePartition analysis. The expression of the top genes along the orderings of the epithelial cells and the stromal cells consistently showed great dynamic changes (Fig. 2d). However, no such pattern was observed for the NK or T cells (Supplementary Fig. 8b).

To avoid biased findings, we further validated the robustness of StemVAE using independent internal samples and public datasets<sup>18</sup>. StemVAE, trained on the 18 donors of the present study, could locate single cells of new LH + 7 endometrial biopsies within the timeframe of LH + 7 (Fig. 2e), and could order single cells from early-/mid-/late-secretory endometrium in a sequential manner regardless of the sequencing platforms (Supplementary Fig. 10). Moreover, a different ordering method psupertime<sup>32</sup> which also takes into time-series as input was applied to our dataset and revealed the distinctions across WOI for the unciliated epithelial cells and the stromal cells, as well as the indistinguishable states for the immune subsets confirming their relative steady molecular profiles across the WOI (Supplementary Fig. 8c).

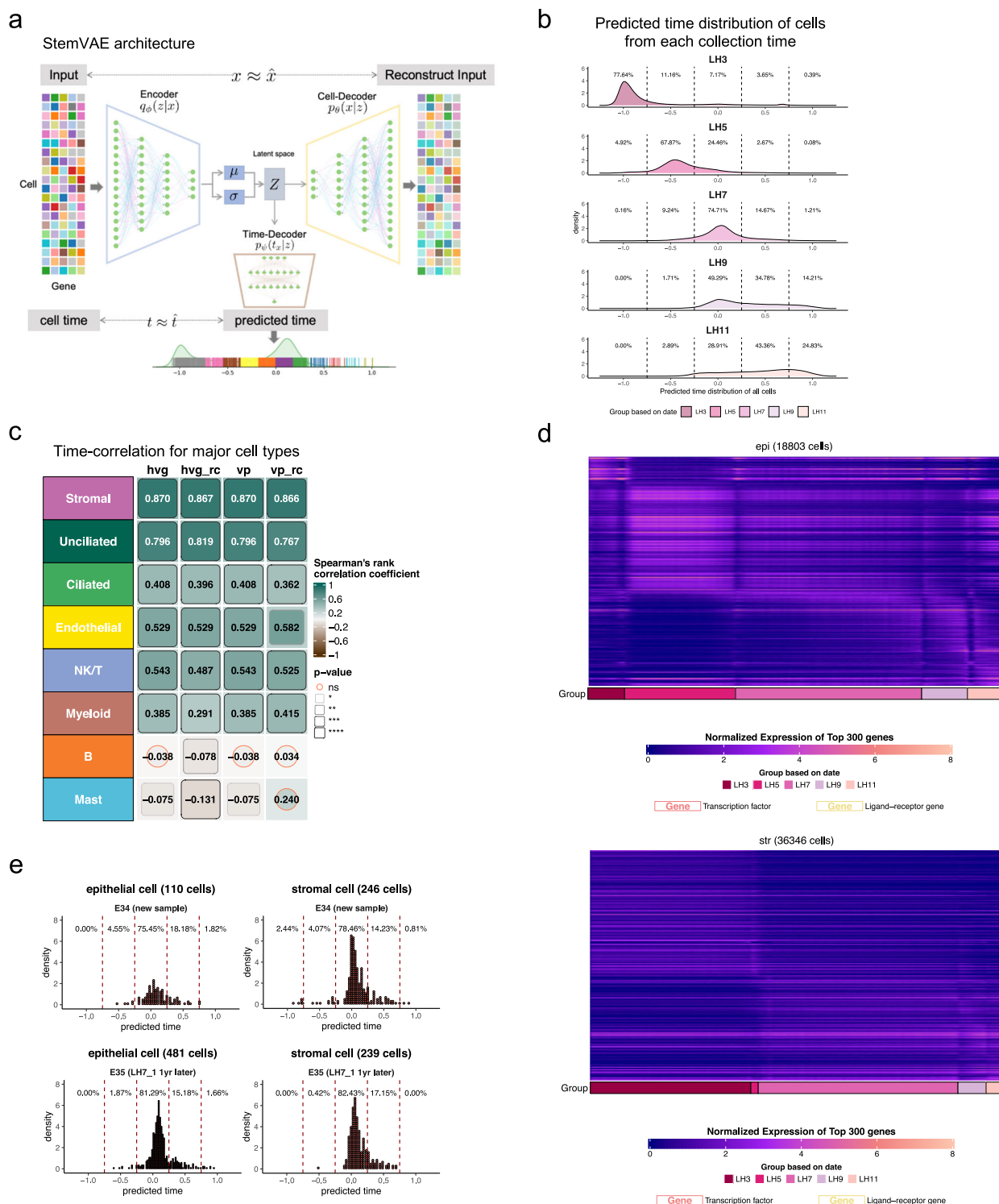


**Fig. 2 | StemVAE reconstruction uncovers endometrial cell time-association across WOI.** **a** Architecture of StemVAE. Composed of a deep nonlinear encoder and two decoders, StemVAE represents single-cell expression data labeled with sampling time into a lower-dimensional latent space for expression and time reconstruction. **b** Predicted time distribution for the fertile controls collected at different time points. A predicted time  $\in [-1, 1]$  was generated by StemVAE for each cell from each individual. Density plots showing predicted time distribution of all cells from samples collected at a given time LH + 3/+ 5/+ 7/+ 9/+ 11. **c** Spearman's rank correlation coefficient of predicted time and sampling time for each major cell type under different training modes of StemVAE. hvg: highly variable genes; rc:

random cell; vp: time-associated genes from variancePartition. Nonparametric Spearman's rank sum test was used.  $P$  values  $\leq 0.05$  were represented as \*,  $\leq 0.01$  as \*\*,  $\leq 0.001$  as \*\*\*,  $\leq 0.0001$  as \*\*\*\*. **d** Heatmap showing the dynamic time-associated gene expression along the time axis for epithelial (top) and stromal cells (bottom). Cells were ordered according to the predicted time within each group. **e** Predicted time distribution for epithelial and stromal cells of independent samples collected at LH + 7 based on the training model on 18 fertile controls. E34 was an independent donor recruited for validation; E35 was the repeated endometrium biopsy of donor LH7\_1 one year later since the first sampling.

## The stromal cells exhibited homogenous actions across WOI

To understand the nature of endometrial receptivity, we separately investigated the functional activities of the stromal cells and the epithelial cells across WOI by dissecting their gene dynamics. Comparison among the time-variable gene sets identified from all the stromal cells together and each subpopulation showed high overlap (Supplementary Fig. 11a), suggesting similar molecular changes across WOI in these cells. Further inspection of the top 500 expressed genes in the three major subpopulations (Str1, Str2, Str3) showed the same changing pattern with an abrupt transition from LH + 5 to LH + 7 (Supplementary Fig. 11b). Therefore, all the stromal cells were regarded as an integral population for the following biological investigation.

In total, 131 genes with MI score greater than 0.1 were identified in the stromal cells (Supplementary Data 2). Ordering these genes based on the time at which the StemVAE predicted the occurrence of their global maximum revealed global features of transcriptomic dynamics across the WOI (Fig. 3a). A clear-cut difference in gene expression between LH + 5 and LH + 7 was observed: a similar gene set was activated at LH + 3 and LH + 5, but a different gene set was activated at and beyond LH + 7. The similarity at transcriptomic level between LH + 3 and LH + 5 endometrium was reported by a previous bulk study<sup>33</sup>. Furthermore, gene subsets with enhanced or suppressed expression at LH + 9 and LH + 11, respectively relative to that of LH + 7 were observed. To determine the main biological processes at each stage, we identified 5 gene clusters based on their expression pattern.

Gene cluster 1 and cluster 2 exhibited high expressions at LH + 3 and LH + 5 and decreased continuously thereafter. These genes were related to genome organization, hedgehog signaling-regulated transcription, cell replication, and production of collagens reflecting initial decidualization (Fig. 3a, Supplementary Data 2, 3). The results revealed that the stromal cells at these time points were molecularly prepared for the transition to WOI by self-expansion and extracellular matrix remodeling. Functional enrichment analysis of Gene cluster 3 was omitted because it contained only two genes. Genes in cluster 4 and cluster 5 were significantly activated from LH + 7 onwards (Fig. 3a). The cluster 4 genes plateau off from LH + 9, while the cluster 5 genes started to decrease after LH + 9. They included well-recognized decidualization regulators such as *FOXO1*, and *CEBPD*, which were highly expressed not only in the LH + 7 cells but also in those at LH + 9 and LH + 11. Decidualization is crucial to embryo invasion and development<sup>34</sup>. The observations indicated widespread and strong activation of stromal cell differentiation for decidualization at the start of WOI (LH + 7) that persisted till a later stage to synchronize with embryo implantation. In addition to genes for decidualization, the two clusters were enriched with genes related to inflammation and immune activities (e.g. *FOXO1*, *STAT3*, *TLR4*), supporting the theory that decidualization creates an inflammatory microenvironment for the early stage of implantation<sup>35</sup>. Interestingly, several inflammation-promoting genes namely *HLA-B/C*, *C3*, and *SERPINE1* showed much-enhanced expression in the LH + 9 and LH + 11 cells (Fig. 3a, Supplementary Data 2, 3), consistent with a two-stage inflammation theory of implantation, i.e. a moderate inflammatory environment is necessary for embryo implantation while an intense inflammation leads to tissue breakdown<sup>35–37</sup>. Particularly, *DKK1*, a natural inhibitor of WNT signaling known to play a role in maintaining and elevating the inflammatory tone of stromal cells<sup>38</sup>, was moderately expressed at LH + 7 and became highly expressed at later time points. Protein-protein interaction network analysis of the pathway-enriched dynamic genes in different clusters (Supplementary Data 3, Supplementary Fig. 12a) explicitly revealed potential essential regulators at each stage. For instance, two decidualization-promoting genes *FOXO1*, and *STAT3* were core regulators in Cluster 4 genes.

Senescent cells in the endometrium are responsible for driving the initial inflammatory response<sup>35</sup>. Here we calculated a senescence score for each cell type according to a published senescent gene set

SenMayo<sup>39</sup> which was validated to indicate endometrium ageing (see Methods, Supplementary Fig. 13) utilizing public datasets<sup>40,41</sup>. The results showed enhanced senescence score (above the 0 line) in the stromal cells and the endothelial cells when compared to epithelial subsets, but only the stromal cells exhibited a strong elevation (fold change of mean value > 3, p-value < 2.2e<sup>-16</sup>) at LH + 7 when compared to those at LH + 5 (Fig. 3b) emphasizing the prominent role of stromal senescence in regulating endometrial inflammation. Dynamically, all the cell types exhibited a higher senescence score at LH + 11 than at LH + 7 in line with the tissue destruction-related inflammation at LH + 11 (Fig. 3b). Consistently, a significant correlation was observed between the senescence score and inflammation score calculated using a gene set of HALLMARK\_INFLAMMATORY\_RESPONSE from MSigDB database<sup>42</sup> in the stromal cells at single-cell level (Fig. 3c). Altogether, the continuous elevation of the senescence score from LH + 7 supported the association between stromal senescence and endometrial inflammation.

## Epithelial cells exhibited heterogeneous actions across the WOI

Unlike the stromal cells, differential time-association were observed for epithelial cells: epithelial cell subtypes namely, glandular, luminal, secretory, and EMT epithelial cells, manifested high Spearman's rank correlation between predicted time and time of the menstrual cycle, whereas the correlation was low for the ciliated, EPCAM<sup>+</sup>SOX9<sup>+</sup>, LGR5<sup>+</sup>, and proliferative (cycling) subpopulations (Supplementary Fig. 8a). The low time-association nature of the ciliated cells found support from a previous finding that the ciliated epithelial cells were present throughout the menstrual cycle and not solely induced by progesterone<sup>19</sup>. Heterogenous activities of the epithelial cells across the WOI were further supported by the low overlap among the significant dynamic genes from each subpopulation as well as the dynamic expression patterns of the top 500 DEGs (Supplementary Fig. 11c, d).

The luminal subpopulation of epithelial cells with both luminal and glandular features (Fig. 1b), encompassed the ability to accept embryo attachment and invasion. In total, 556 genes with MI scores greater than 0.1 in this subpopulation were used for the construction of temporal dynamics and gene clustering (Supplementary Data 2). The genes were ordered in the same way as that of the stromal cells. Different from the stromal cells, a gradually changing expression pattern along the time axis was observed (Fig. 4a). Five gene clusters with different temporal expression patterns were identified. Functional enrichment analysis revealed high metabolic activities like fatty acid metabolism, xenobiotic metabolism, and late estrogen response at the initial stage (Cluster 1 and 2), followed by apoptosis, epithelial-mesenchymal transition, mineral absorption, and initial inflammation at the mid-stage (Cluster 3 and 4), and subsequent wide inflammatory responses, cellular senescence, and protein metabolism at the late stage (Cluster 5) (Fig. 4a, Supplementary Data 3). The regulatory relationship within each stage was constructed (Supplementary Fig. 12b). In the dynamic ranking gene list (Fig. 4a, Supplementary Data 2), the two female sex steroid receptors *PGR* and *ESR1* peaked at the initial stage (LH + 3 and LH + 5) highlighting their critical roles in early preparation of the WOI (Cluster 1). The possible antigen-presenting role of epithelial cells was interestingly noted by the expression of non-classical MHC class II genes like *HLA-DOB* before the opening of the WOI (Cluster 2, Supplementary Data 2). On the contrary, peak expressions of reported receptivity-related genes *CXCL14*, *PAEP*, *GPX3*, and *DPP4* were mostly at or towards LH + 11 (Cluster 5) suggesting their main functions were on embryo invasion rather than on embryo adhesion. The increasing expression pattern of these receptivity-related genes from early to late secretory stages was also reported in another study using bulk RNA sequencing<sup>31</sup>.

Among genes of Cluster 2, some of them peaked around the WOI among which several transcription factors including *CREB3L1*, *PAX2*,



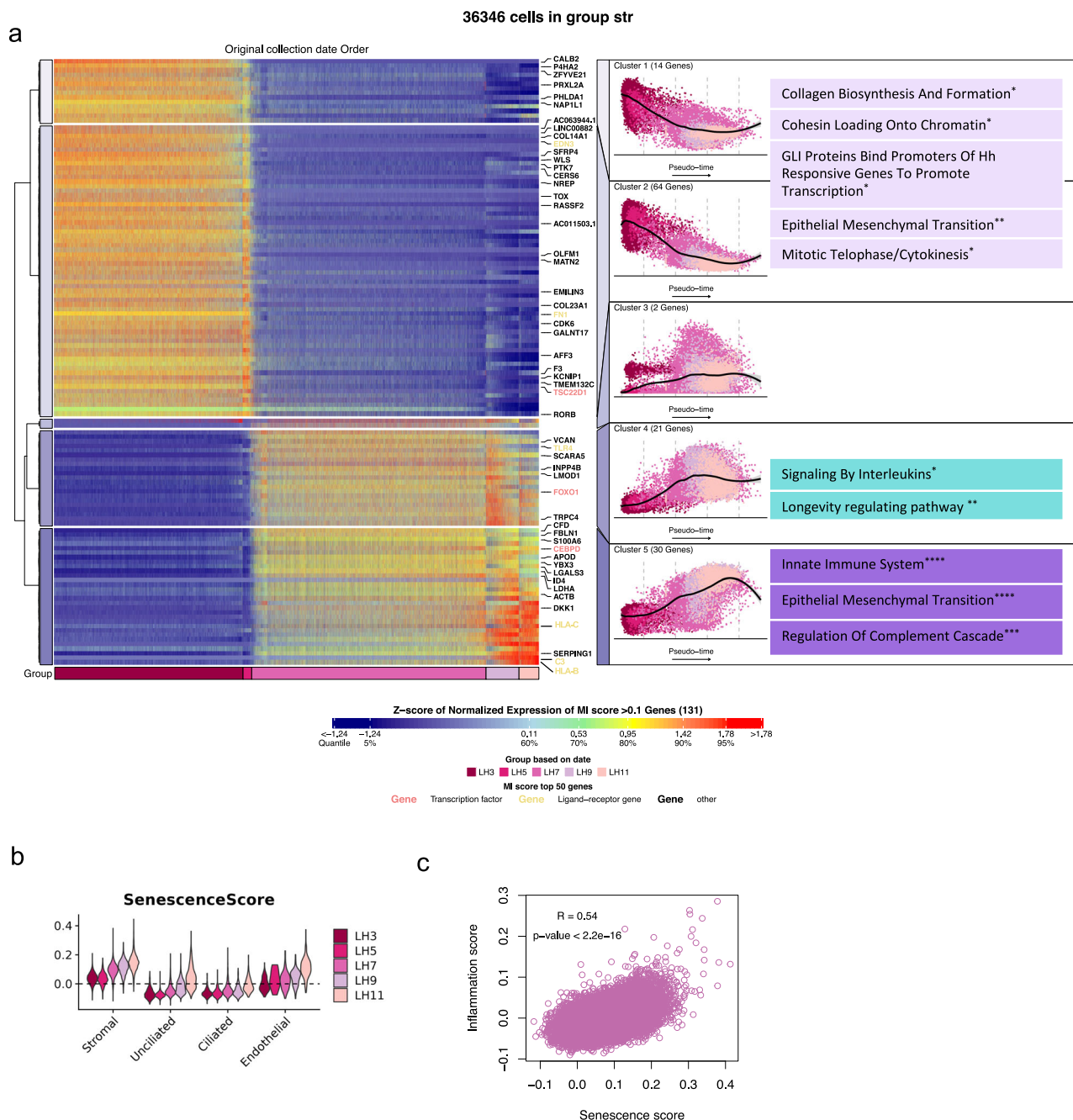


**Fig. 3 | Characteristics of stromal dynamics across the window of implantation.**

**a** An integrated scheme showing the heatmap of denoised and scaled expression of time-associated genes in stromal cell (left), expression trend of each gene cluster (middle), and significantly enriched biological terms/pathways from KEGG, Reactome, and MSigDB Hallmark (right). The color scale of heatmap represents the Z-score of normalized expression of included genes in the heatmap. Fisher exact test with Benjamini–Hochberg adjust was used for enrichment analysis. *P* values

$\leq 0.05$  were represented as \*,  $\leq 0.01$  as \*\*,  $\leq 0.001$  as \*\*\*,  $\leq 0.0001$  as \*\*\*\*. Exact *p* values can be found in Supplementary Data 3. **b** Violin plot showing the distribution of senescence score of stromal, epithelial, and endothelial cells across WOI.

**c** Scatter plot showing the significant correlation relationship between senescence score and inflammation score. Pearson's correlation test at 95% confidence interval was used.

*RORA*, *SOX5*, and *NFIB* were identified (Fig. 4a, b, Supplementary Data 2). Their roles in preparation for the WOI remain to be investigated. Genes of Cluster 3 peaked at the start of WOI and decreased thereafter, whereas genes of Cluster 4 peaked at late LH + 7 and then plateaued off (Fig. 4a). The relevance of these two Clusters to WOI was reflected by the presence of genes known to be important in implantation. For instance, *FOXO1* of Cluster 3 is a progesterone receptor-regulated core transcription factor for endometrial remodeling and embryo implantation<sup>43,44</sup>. Interestingly, with the use of a transcription factor binding sites database (<https://tfbsdb.systemsbio.net/>)<sup>45</sup>,

32.2% of the genes were found to be the potential targets of *FOXO1*, supporting its mastery role in regulating the expression of implantation-related genes. Indeed, uterine-specific knockout of *FoxO1* disrupted the polarity of endometrial luminal epithelial cells and embryo penetration, causing infertility in mice<sup>46</sup>. Cluster 4 contained known implantation regulator *CDH1*<sup>47,48</sup> and *CD44*<sup>49</sup> (Fig. 4b). We also found significant elevation of the expressions of a cluster of metallothionein genes (*MTIG*, *MTIE*, *MT2A*, *MTIM*) at LH + 7 (Fig. 4b) consistent with a previous study using bulk RNA-seq<sup>50</sup>. The expression patterns of *CDH1* and *MTIX* were validated by qPCR in primary

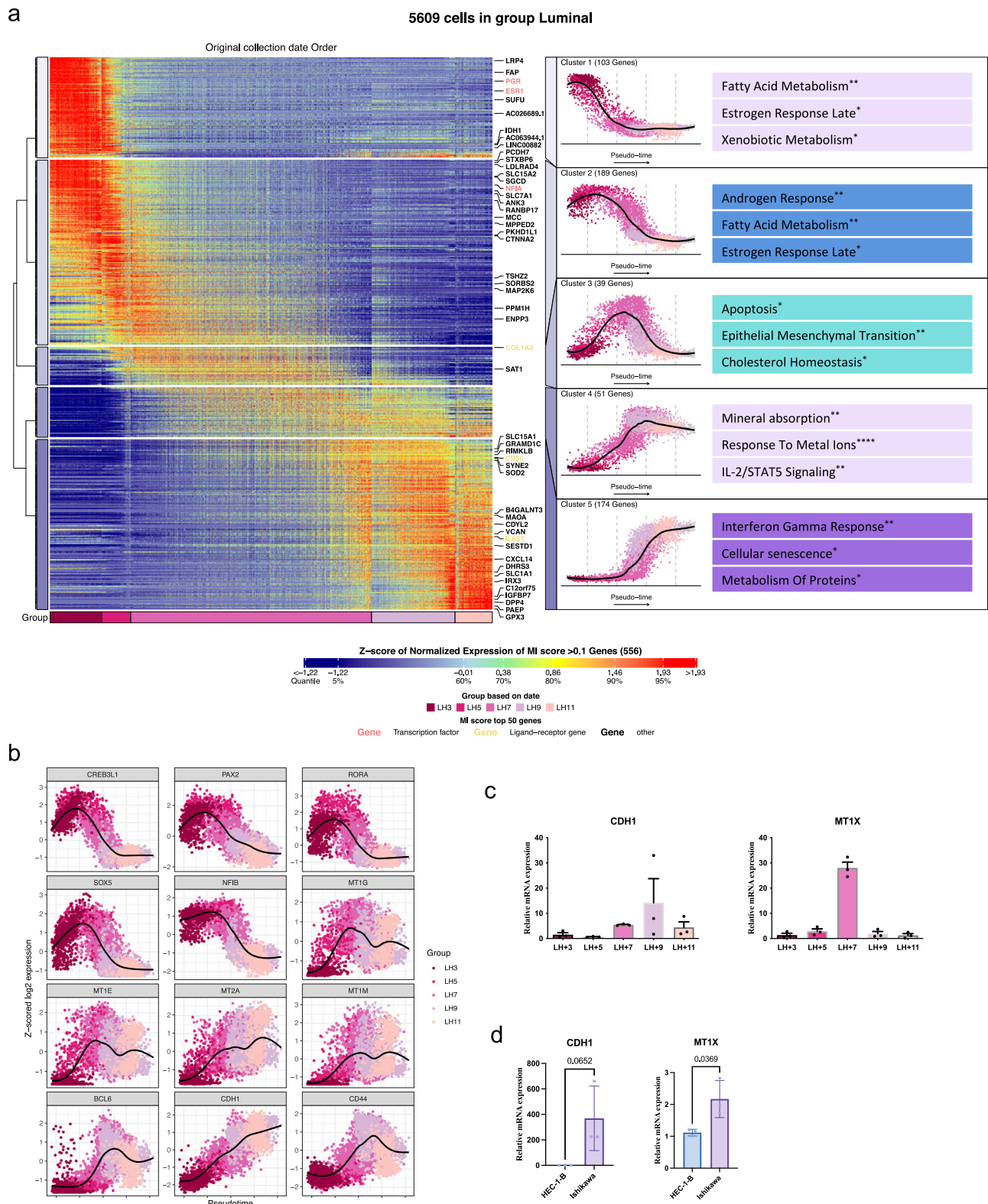


**Fig. 4 | Characteristics of epithelial dynamics across the window of implantation. a** An integrated scheme showing the heatmap of denoised and scaled expression of time-associated genes in luminal epithelial cell (left), expression trend of each gene cluster (middle), and significantly enriched biological terms/pathways from KEGG, Reactome and MSigDB Hallmark (right). The color scale of heatmap represents the Z-score of normalized expression of included genes in the heatmap. Fisher exact test with Benjamini–Hochberg adjust was used for enrichment analysis.  $P$  values  $\leq 0.05$  were represented as \*,  $\leq 0.01$  as \*\*,  $\leq 0.001$  as \*\*\*,  $\leq 0.0001$  as \*\*\*\*. Exact  $p$  values can be found in Supplementary Data 3. **b** Expression

trend of selected transcription factors, unreported, and known epithelial receptive genes. **c** Expression validation of candidate receptive genes CDH1 and MT1X across WOI. For each group, independent samples ( $n = 3$ ) were included. Data are presented as mean values  $\pm$  SEM. **d** Increased expression of CDH1 and MT1X in receptive Ishikawa cells compared with non-receptive HEC-1-B cells. For each group, independent samples ( $n = 3$ ) were collected. Data are presented as mean values  $\pm$  SD. Two-sided Student's  $t$  test was used with 95% confidence interval. Source data are provided as a Source Data file.



endometrial tissues at the aforementioned time points (Fig. 4c) as well as in a receptive (Ishikawa) and a non-receptive (HEC-1-B) endometrial epithelial cell line (Fig. 4d). The wide expression of genes from Cluster 3 and Cluster 4 in most of LH + 7 cells were suggestive of their roles in regulating embryo adhesion and initial invasion.

Similar analyses were conducted on the glandular and secretory epithelial cell subpopulations. Different dynamic expression patterns were observed (Supplementary Fig. 14, Supplementary Data 2). Similar to the stromal cells, a sharp transitional process from LH + 5 to LH + 7 was observed in the glandular epithelial cells (Supplementary Fig. 14a). For the secretory epithelial cells, a sharp transition was observed at late LH + 9 (Supplementary Fig. 14b) suggesting an activation mechanism different from that of the glandular epithelial cells and the stromal cells. Gene cluster identification and functional enrichment analysis were performed and revealed general dynamic activities across the WOI: protein synthesis and active metabolism in the initial stage, followed by cell death and metabolism, and at last cell death and inflammatory responses (Supplementary Fig. 8, Supplementary Data 3).

### Stromal cells and epithelial cells collectively shape the immune microenvironment during WOI

StemVAE prediction analysis revealed a time-invariant property of the immune cells, which was reasonable as the immune cells had completed their principal identity commitment during hematopoiesis. Their changes across WOI therefore would be subtle involving mainly in immune cell maturation and immune responses. Among the time-varying genes in the epithelial cells and the stromal cells, cell-cell interacting molecules such as chemokines were identified (Fig. 5a, d, Supplementary Fig. 15a, b) suggesting their role in shaping the immune microenvironment across the WOI. To decipher how the stromal cells and the epithelial cells dynamically affect the immune microenvironment, we first performed cell-cell communication (CCC) analysis at each time point. The results indicated extensive CCC between the stromal cells and the immune cells, which was much stronger than that between the unciliated epithelial cells and the immune cells. This suggested a predominant role of the stromal cells in modulating immune functions (Supplementary Fig. 15c). Spatial proximity between the interacting cells can help reduce false positive CCC pairs. By utilizing spatial transcriptomic data of secretory endometrium<sup>19</sup>, spatially co-expressed CCC pairs were identified. Among the significant CCC pairs with spatial proximity, we identified 13 and 11 significant time-associated molecules from the stromal cells and the epithelial cells, respectively that might interact with the immune cells (Fig. 5b, e). Expression analysis of the interacting molecules in the lymphocyte and the myeloid subsets showed differential expression for some of them (Supplementary Fig. 15d, e). Several stromal-immune pairs (*CXCL12-CXCR3/4*, *ANXA1-FP1/3*, *HLA-C-FAM3C*, *C3-ITGB2/ITGAM*, *CD55-ADGRE5*) and epithelial-immune pairs (*TGFB2-TGFBRI/2*, *SPPI-CD44*, *ANXA1-FP1/3*, *CDH1-ITGB1/ITGAE*, *CD55-ADGRE5*) were noted for their co-expression and interactions in the WOI (Fig. 5c, f, Supplementary Fig. 16). For instance, the stromal cell-specific *CXCL12* and high expression of *CXCR4* on the NK/T and myeloid cells suggested modulation of the endometrial immune microenvironment by stromal cells (Fig. 5b, c). The epithelial cells expressed *TGFB2*, which might interact with *TGFBRI* and *TGFBRI2* on the NK/T and myeloid cells to exert its immunosuppressive functions (Fig. 5e, f). On the other hand, the immune cells might also modulate endometrial cell functions. For example, *CDH1* on the epithelial cells is an interacting partner of integrins expressed in the immune cells (Fig. 5e).

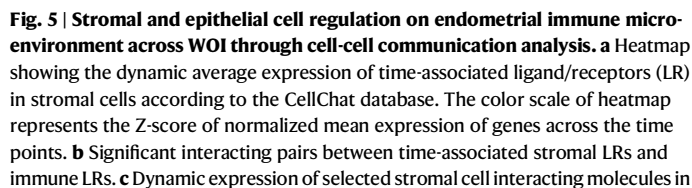
### Epithelium dysfunction in a hyper-inflammatory environment of RIF endometrium

Displacement of WOI and pathogenic changes of the endometrium are two potential causes of RIF<sup>17</sup>. In total, we profiled 90,754 cells from 10

RIF endometria at LH + 7, which were compared to 45,282 endometrial cells from 6 fertile women at LH + 7 (Fig. 6a). Similar cell types were observed in the two groups (Figs. 1b and 6a). To evaluate possible displacement of WOI in the RIF endometrium, StemVAE was applied to determine the developmental status of the endometrial epithelial cells and stromal cells (Supplementary Fig. 17a). Hierarchical clustering of the percentage of in-frame cells showed segregation of the 10 RIF samples into 2 groups (Fig. 6b). Specifically, partial epithelial cell displacement to LH + 9 in RIF-4, RIF-8, RIF-10 and stromal cell displacement to LH + 9 in RIF-8 and RIF-10 were observed accounting for 30% of the RIF samples consistent with previous reports<sup>51,52</sup>. Therefore, we divided the RIF samples into two classes (RIF-4, -8, -10 as RIFClass1, and the remaining as RIFClass2) for pathogenic factor identification. Utilizing the pre-defined gene clusters responsible for stromal decidualization (stromal cluster 4 and cluster 5 in Fig. 3a) and epithelial receptivity (epithelial cluster 3 and cluster 4 in Fig. 4a), an overall gene set activity score for each cluster was calculated at the single-cell level and the mean scores of each donor were compared among the LH7, RIFClass1, RIFClass2 groups. No significant difference was observed for the stromal decidualization score and senescence score. However, an increasing trend of decidualization and senescence score was still observed for RIFClass1 supporting their displacement to a later WOI. The RIFClass1 exhibited a significant reduction in the epithelial receptivity score for the Cluster 3 genes, while the RIFClass2 showed a reduction of score for the Cluster 4 genes when compared to the fertile controls (Fig. 6c, Supplementary Fig. 17b). It was noted that the expression of cluster 3 genes in epithelial cell was high only in early LH + 7 suggesting possible involvement in early implantation. The WOI-displaced RIFClass1 showed reduced receptivity activity of epithelial cluster 3 involving early implantation, while RIFClass2 without WOI displacement exhibited reduced receptivity activity of epithelial cluster 4 involving in late implantation (invasion). The observations suggested epithelial defects as the main cause of RIF.

To identify the most dysregulated epithelial genes in the RIF endometrium, we only considered the common genes from the following criteria: (a) significant differentially expressed genes (DEGs) between RIF and fertile endometrium at LH + 7 with fold change greater than 1 (Supplementary Figs. 18, 19, Supplementary Data 4); (b) features selected by the random forest algorithm for classification of the RIF endometrium relative to the control endometrium (Supplementary Fig. 17c, Supplementary Data 4); and (c) time-associated genes with significant variation (Supplementary Fig. 17d, Supplementary Data 2). In total, 45 genes were identified for RIFClass1 and 23 genes for RIFClass2, among which 9 (*ACO24230.1*, *CRISP3*, *CTNNA2*, *DEFB1*, *MT-CO1*, *MT-ND3*, *NEAT1*, *S100P*, *SCGB1D2*) were shared by both classes (Supplementary Data 4, Supplementary Fig. 17e). External scRNA-seq datasets of RIF further validated the dysregulation of these genes in epithelial cells (Supplementary Fig. 20).

We also studied the DEGs in other cell subtypes between the RIF and the fertile endometria, the highest number of dysregulated genes were observed in the myeloid cells (Supplementary Figs. 18, 19) suggesting the existence of differential inflammatory activities in the two groups. Inflammation score analysis showed that the strongest inflammatory responses in endometrium were attributed to the myeloid cells (Supplementary Fig. 21a). The enrichment of myeloid cells in the RIF endometrium (Supplementary Fig. 21b) indicated a hyper-inflammatory microenvironment in RIF. To determine whether the hyper-inflammation was a potential cause of the epithelial dysfunction in RIFClass2, we performed functional enrichment analysis on the RIFClass2-upregulated genes and found wide enrichment of interferon gamma response in the endometrial cells and immune cells (Fig. 6d). IFNG was mainly expressed in the NK cells and the T cells (Fig. 6a, e, Supplementary Fig. 21c) and its expression was increased in the RIFClass2 endometrium relative to the fertile endometrium (Fig. 6f, Supplementary Fig. 21d). IFNG treatment of



NK/T and myeloid cells. **d** Heatmap showing the dynamic average expression of time-associated ligand/receptors (LR) in luminal epithelial cells according to the CellChat database. The color scale of heatmap represents the Z-score of normalized mean expression of genes across the time points. **e** Significant interacting pairs between time-associated epithelial LRs and immune LRs. **f** Dynamic expression of selected epithelial interacting molecules in NK/T and myeloid cells. Partially created in BioRender. Gong (2024) <https://BioRender.com/g77u078> (c, f).

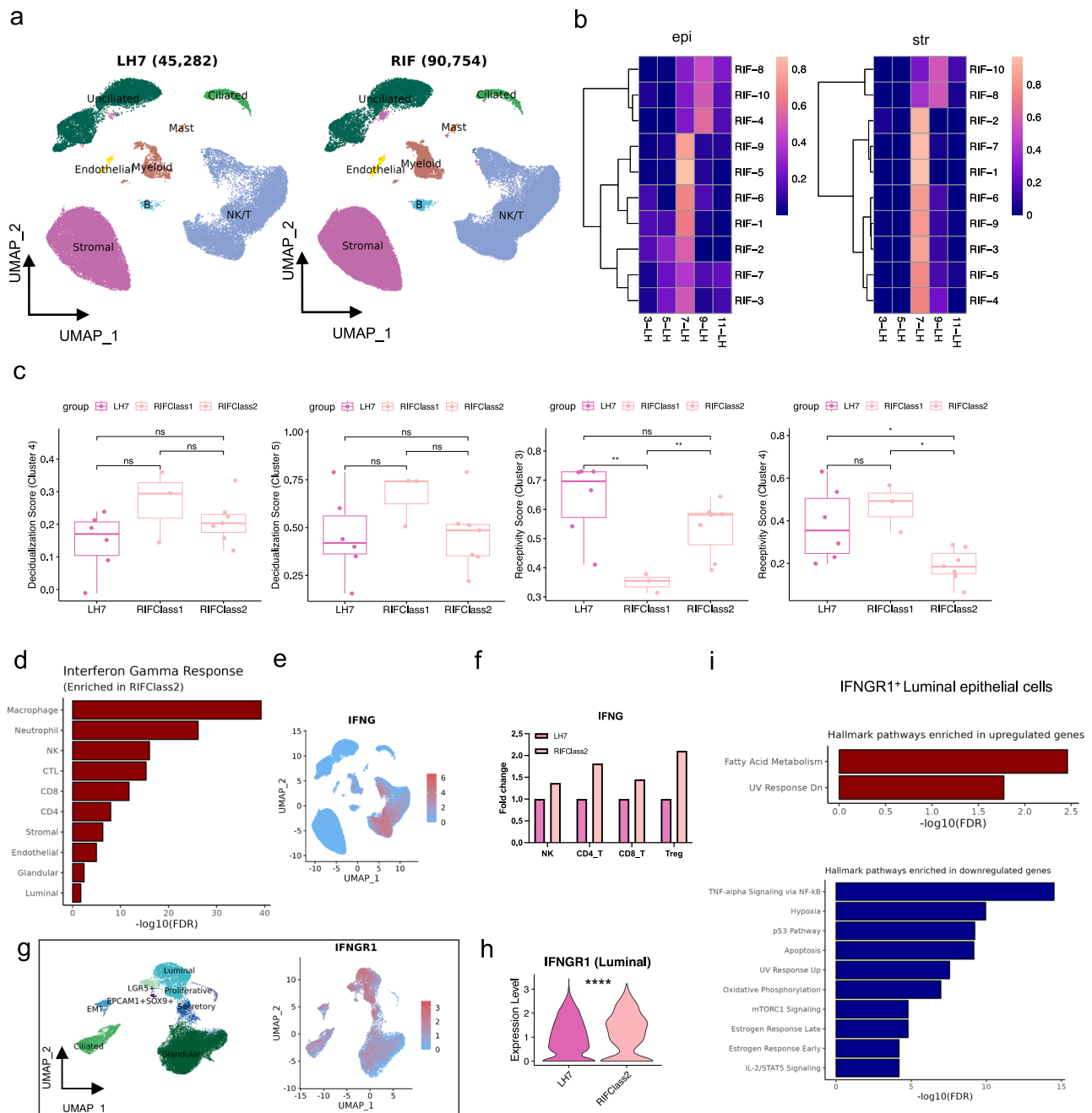


**Fig. 6 | Pathological endometrial characteristics of RIF patients at WO1.** **a** UMAP plots of 45,282 cells in the fertile LH7 group and 90,754 cells in the RIF group showing the major cell types. **b** Heatmap showing the clustering of RIF patients based on the cell percentage distribution of epithelial and stromal cells predicted by StemVAE. Window displacement (from LH + 7 to LH + 9) could be seen in the RIF endometrium. The color scale of heatmap represents cell percentage. **c** The estimated decidulization score in stromal cells and receptivity score in epithelial cells using respective gene sets between fertile (*n* = 6) and RIF endometrium (*n* = 3 for RIFClass1, *n* = 7 for RIFClass2). N indicates independent samples. The boxes extend from the first quartile (Q1) to third quartile (Q3), with the band inside the boxes representing the median. The whiskers extend to the smallest and largest values within 1.5 times the inter-quartile range (IQR), where IQR is the difference between Q3 and Q1. The two-sided Student's *t* test was used to determine the statistical

significance, *p* values ≤ 0.05 were represented as \*, ≤ 0.01 as \*\*. **d** The GSEA hallmark pathway (Interferon gamma response) enriched in RIFClass2-derived cells, ordered by -log10(FDR). **e** UMAP plot of IFNG expression in fertile and RIF cells. The color scale represents normalized gene expression. **f** Fold change of IFNG expression between fertile and RIFClass2 derived NK, CD4<sup>+</sup>T, CD8<sup>+</sup>T and Treg cells. **g** UMAP plot of IFNGR1 expression in fertile and RIF-derived epithelial cells. **h** Violin plot of IFNGR1 expression between fertile and RIFClass2 derived luminal epithelial cells. Two-sided *t* test at 95% confidence interval was used. *P* values ≤ 0.0001 were represented as \*\*\*\*. **i** The GSEA hallmark pathways (ordered by -log10(FDR)) enriched for upregulated genes (upper panel) and downregulated genes (lower panel) in RIFClass2-derived IFNGR1<sup>+</sup> luminal epithelial cells when compared to that of fertile women. Source data are provided as a Source Data file.

ISHIKAWA cells decreased the trophoblast organoid attachment rate (Supplementary Fig. 21e). The expression of IFNG receptor, *IFNGR1*, was high in the luminal epithelial cells (Fig. 6g) and was significant elevated in the RIFClass2 (Fig. 6h). The dysregulated functions of

IFNGR1-positive luminal epithelial cells in RIFClass2 were mainly involved in receptivity regulating pathways such as fatty acid metabolism, estrogen responses, oxidative phosphorylation (Fig. 6i) as revealed in Fig. 4a. Altogether, we identified epithelium dysfunction



as the major contributor of RIF pathogenesis which was strongly associated with a hyperinflammation microenvironment.

## Discussion

In this study, we comprehensively characterized the dynamic transcriptomic changes of precisely timed human endometrium at single-cell level across the WOI in high coverage and deciphered the pathologic factors of RIF endometrium. Our analyses yield a comprehensive catalog of endometrial cells enabling identification of major and rare cellular subsets and exploration of endometrial receptivity in normal and disease conditions. With the 130,094 single-cell data of 18 endometrium biopsies from fertile women, we report the distinct dynamics of the stromal cells and the epithelial cells across the WOI. The stromal cell dynamic is characterized by extensive replication and ECM remodeling before initiation of the WOI, followed by an intensive decidualization process, during which stromal senescent cells exhibited significant correlation with inflammation and manifested metabolic and immune regulatory crosstalk. On the other hand, the epithelial subpopulations exhibited heterogeneous temporal dynamics across the WOI. With StemVAE, we identify epithelial receptivity gene sets and show that displacement of WOI and reduced epithelial receptivity in a hyper-inflammatory environment are correlated with RIF.

Single-cell order estimation is critical for deciphering dynamics. Our data is a time-series dataset that provides prior time information. Current computational techniques rarely infer time series-specific transcriptomic changes. Therefore, we developed StemVAE which predicts the time of a cell via a multilayer neural network preserving the temporal characteristics of cells. StemVAE is flexible and effective for large datasets making it superior to the existing supervised pseudotime estimation method *psupertime*, which utilizes an ordinal logistic regression model<sup>32</sup>. StemVAE successfully established the single-cell order of endometrial samples from normal fertile population across the WOI which preserved the time-series information. StemVAE trained on fertile samples was able to predict single-cell time domain distribution for newly collected samples. The invariant of time domain distribution for LH + 7 samples from the same donor collected in different menstrual cycles spanning one year allowing the application of StemVAE for WOI displacement prediction for pathological samples. The small cycle-to-cycle variance of endometrium was also reported in a previous bulk study<sup>53</sup>.

Our time-series data across the WOI revealed complex cellular heterogeneity in endometria and large inter-individual variations in cellular composition at the same time point despite standardized timing for sample collection. The heterogeneity was simultaneously observed in populations with or without prior pregnancy history (Supplementary Data 1). Prior pregnancy history not impacting endometrial receptivity was also indicated by studies with large sample size which showed no association of previous eutopic pregnancy with IVF outcome such as 'live birth rate'<sup>54,55</sup>. While the pregnancy history effect was to some extent ruled out, it remains possible that the cellular heterogeneity might be due to the similar rather than the 100% precise sampling timing which is notoriously challenging. The observations caution the cell abundance analysis for human endometrium, and help to explain contradictory results in previous studies that profiled immune cell percentages, such as uterine NK cells in RIF, with limited sample size<sup>56–58</sup>.

Although the data was collected from endometria in the secretory phase, we identified epithelial progenitor subpopulations, the EPCAM<sup>+</sup>SOX9<sup>+</sup> (MUC5B<sup>high</sup>), and the LGR5<sup>+</sup> cells. Their basalis and luminal surface location supported the previous suggestion that the LGR5-rich lumen is a second endometrial stem cell niche other than the basalis stem cell pool<sup>27,29</sup>. The luminal epithelial cells likely contribute to glandular regeneration in the functionalis layer of the endometrium. Supportively, the identified luminal epithelial subpopulation exhibited

glandular characteristics and was localized to both the epithelial surface and glands. In addition, the other reported luminal epithelial cell marker EDG7 (*LPAR3*)<sup>26</sup> was also detected in both the luminal surface and the newly formed glands in proliferative phase endometria. Nevertheless, future single-cell lineage tracing is critical to confirm the contribution of the luminal epithelial cells to the regeneration of endometrial glands.

Stromal cells and epithelial cells are two major functional cell types essential for endometrial receptivity. In this study, both cell types exhibited great molecular changes across the WOI. Of interest, the stromal cells manifested a sharp activation of decidualization coinciding with embryo implantation at LH + 7. The differentiation process manifested with stromal senescence and inflammation which could be further divided into two waves: moderate inflammation at mid-secretory stage and intense inflammation at late-secretory stage. These observations find support in previous reports<sup>34,35</sup> and render human endometrium as a natural aging model. Here, we further suggest that the driver for stromal senescence at LH + 7 might be the replicative stress during the strong replication/transcription events before LH + 7. Although stromal senescence significantly correlated with inflammation across the WOI, the direct tuning together with the tuning mechanisms of inflammation in the endometrium by the senescence of stromal cells requires further validation and investigation. Interestingly, a recent report showed that the release of mitochondrial DNA (mtDNA) into cytosol plays a role in the induction of inflammation during senescence<sup>59</sup>. Consistently, our data showed enriched metabolism and oxidative activities in the stromal cells during decidualization suggestive of strong mitochondria responses. Whether mtDNA is produced and as the driver for endometrial inflammation is worthy of future exploration.

Unlike the stromal cells, the luminal epithelial cells exhibited a gradual transitional process across the WOI. By dynamic gene expression analysis, two clusters of genes coinciding early (luminal epithelial cluster 3) and late (luminal epithelial cluster 4) embryo implantation were proposed as epithelial receptivity genes which were functionally supported by their enrichment in known receptivity-related pathways such as mineral absorption<sup>60</sup>, androgen responses<sup>61</sup>, and EMT<sup>62</sup>. The importance of the gene set to implantation was also supported by its inclusion of some known receptivity genes such as *FOXO1*, *CDH1*, and *CD44*. In particular, the core transcription factor *FOXO1* can potentially regulate the expression of a significant proportion of the Cluster 3 and 4 genes. Importantly, a family of metallothionein genes was consistently found by us and others to be highly expressed in normal WOI<sup>60</sup> but decreased in the pathologic endometrium of Asherman's syndrome<sup>23</sup>. However, their exact function in embryo implantation is still unknown and future exploration is warranted.

A previous study reported different dynamic patterns of endometrial cells across the WOI; a widespread decidualization of the stromal cells and an abrupt and discontinuous activation of the epithelial cells<sup>18</sup>. The discrepancy may be caused by insufficient sample coverage before the WOI and on LH + 9 in the previous study as indicated by StemVAE prediction of the time distribution of the cells in the study (Supplementary Fig. 10a). Moreover, the study defined WOI by several markers like *PAEP*, *GPX3*, *DPP4*, which were found to have high expression also at the late secretory stage in our study as well as another study<sup>31</sup> suggesting inappropriate WOI dating. But on the other hand, it cannot be ruled out that the discrepancy might be caused by the patient characteristics especially the hormonal milieu in the two cohorts of different ethnic background. The lack of hormonal information at the sampling time in these two studies hindered the further comparison analysis. Future endometrial receptivity studies with companion hormone levels are advocated. On the whole, our study provides a single-cell atlas of high coverage across the WOI which supplements the previous study and enables a more accurate interpretation of the WOI.

The dynamic features of epithelial cell and stromal cell across the WOI, the newly developed StemVAE, together with the small cycle-to-cycle variance of endometrial molecular characteristics enable the endometrial receptivity prediction at single-cell level. By applying StemVAE to RIF endometrium, WOI displacement could be identified according to epithelial cell and stromal cell time domain distribution. Strong post-receptive displacements were observed for 3 out of 10 RIF patients, a similar out-of-phase percentage to previous RIF studies using bulk endometrial receptivity test<sup>51,52</sup>. Pre-receptive or post-receptive preference of RIF patients is not conclusive currently across different studies. As StemVAE predicted time for single cells, the percentage distribution in different time intervals were used for clustering; and the displacement classification was based on the clustering tree which should be improved in future by including larger sample size as well as taking pregnancy outcome into consideration for cutoff setting. Single-cell receptivity estimation resolves the problem of tissue heterogeneity; and would benefit the precise development of clinical treatment. However, the direct comparison of single-cell receptivity estimation versus bulk-level receptivity estimation is further warranted in the future to testify their translational use. Moreover, the lack of hormone levels for each donor at the sampling timepoint hindered the in-depth analysis about the impact of hormone level on endometrial receptivity in the current study.

The two clusters of receptivity genes identified based on the epithelial dynamics are related to dysfunction of the RIF endometrium and can stratify the RIF endometrium into two classes, namely displacement of WOI and in-phase WOI with reduced epithelial receptivity. Although stromal senescence and decidualization have been implicated in reproductive failures such as recurrent pregnancy loss<sup>24</sup>, the overall senescence and decidualization gene set activation analysis did not show a significant difference between fertile and RIF endometria probably due to heterogeneous etiologies of RIF or limited sample size in the present study. Instead, we observed hyper-inflammatory responses such as wide interferon-gamma response in the in-phase RIF endometrium. Inflammation or infection was reported to be one of the endometrial factors for RIF<sup>63</sup>. Moreover, the top dysregulated genes (Supplementary Fig. 17e) found in RIF involving stress and immune response indicated the link between hyperinflammation and reduced epithelial receptivity. Although the hyperinflammation of RIF endometrium might be a cause of abnormal progesterone signaling, their cause-and-effect relationship remains elusive since progesterone was implicated in the regulation of endometrial inflammation<sup>64</sup>. Utilizing data from previous studies<sup>65,66</sup>, dysregulated genes including *CLDN4*, *CXCL14*, *DEFB1*, *GNLY*, *GPX3*, *FAM13A* in the in-phase RIF were found to be potential PR targets and have roles in inflammation modulation. However, we didn't have the progesterone level of these patients for further analysis. Here, we again appeal that progesterone level determination should be a companion in all endometrial studies. In our data, both the stromal cells and the epithelial cells interact with the immune cells. Ligands or cytokines from the stromal cells and epithelial cells can modulate the immune cells expressing the corresponding receptors or vice versa, and several stromal-immune and epithelial-immune interacting pairs including *CXCL12-CXCR3/4*, *TGFB2-TGFBRI/2*, and *CDH1-ITGB1/ITGAE* were identified. Some of these identified interacting pairs were found to be decreased or increased in in-phase RIF endometrium (Supplementary Fig. 22). Their functional implications in RIF pathogenesis require further study. Concerning RIF, we found excessive IFNG transcriptomic expression in the NK/T cells and upregulated *IFNGR1* expression in the luminal epithelial cells with compromised receptivity in the in-phase RIF endometrium. Although the increased transcriptomic and protein expression of Interferon gamma was previously detected in RIF endometrium<sup>67</sup> and peripheral blood<sup>68</sup>, respectively, direct IFNG protein detection in RIF endometrial immune cells should be warranted in the future. Further mechanistic study

linking hyperinflammation, epithelial function, and embryo implantation is worthy of much attention.

In summary, our study supplemented previous limited understanding of the normal dynamics of endometrial receptivity and the factors contributing to implantation failures. This atlas together with the computational framework represents an important tool for the instrumental design of diagnosis panels and therapeutic targets for reproductive failures.

## Methods

### Ethics and study subjects

This study was approved by the Ethics Committee of the University of Hong Kong-Shenzhen Hospital (IRB reference number [2021]173-001) and was conducted according to all relevant ethical regulations. Informed written consent was obtained from each donor after full counseling before an endometrial biopsy was performed. The donors received compensation for participating this study.

The fertile control donors (Supplementary Data 1) included volunteers from the public who had a normal live birth through spontaneous conception within the past 2 years as well as in vitro fertilization (IVF) patients with no female factors and had a live birth after transfer of one normal euploid blastocyst because of a known genetic problem (PGT treatment for monogenic mutation or chromosomal structural variant). The inclusion criteria of the fertile controls were 20–36 years old, BMI 19–25 kg/m<sup>2</sup>, regular menstrual cycle of 25–35 days, normal karyotype except 2 donors for PGT with known chromosomal structural variant, absence of obvious endometrial defects and endocrine or systemic diseases. In total, 15 fertile controls from the public and 3 fertile controls from the IVF center at the University of Hong Kong-Shenzhen Hospital were included in this study. The donors of the RIF group (Supplementary Data 1) were recruited from the IVF center. They were 20–38 years old, with a BMI 19–25 kg/m<sup>2</sup>, exhibiting a regular menstrual cycle of 25–35 days. These individuals experienced implantation failures after transfer of at least 6 good-quality cleavage-stage embryos or 3 high-quality blastocysts within a minimum of three fresh or frozen cycles<sup>69</sup>. Additionally, they showed no obvious endometrial defects and endocrine or signs of systemic disease. For both groups, women with the following conditions were excluded: recent contraception (use of the intrauterine device in the past 3 months or hormonal contraceptives in the past 2 months), recent antibiotic treatment in the past 3 months and uterine pathology (endometriosis, leiomyoma or adenomyosis; hydrosalpinx; bacterial, fungi, or virus infection).

### Tissue collection

Endometrial biopsy in a natural cycle was conducted for both fertile control and RIF subjects under the guidance of the abdominal ultrasound. Specifically, the Pipelle catheter was placed to the uterine fundus followed by fully suction along with in-cavity spinning and then moving downward to the internal cervical ostium. All biopsies were performed by the same doctor (YF.C.) with standard operation to minimize variation. The biopsy days were determined by daily measurement of serum LH level together with E<sub>2</sub> and P<sub>4</sub> when the diameter of the dominant ovarian follicle was >14 mm. The LH surge day was defined as the day with the surging serum LH level together with decreasing E<sub>2</sub> and increasing P<sub>4</sub> levels. Once the surge day was determined, hormone levels would no longer be measured for all the donors. LH surge day was denoted as day LH + 0. Biopsy at LH + 3 was conducted 72 h post LH + 0. The simple day count calculation method was also applied to biopsy schedule for other timepoints. The fertile controls from the public were randomly assigned to five-time points covering LH + 3 (*n* = 3), LH + 5 (*n* = 3), LH + 7 (*n* = 3), LH + 9 (*n* = 3), and LH + 11 (*n* = 3) and subjected to endometrium biopsy accordingly. The fertile PGT patients (*n* = 3) and RIF donors (*n* = 10) had endometrial biopsy done only on LH + 7. For each donor in a natural cycle, no luteal

phase supplementation was given, and endometrial thickness was assessed through transvaginal sonography before endometrial biopsy. All the biopsies were subjected to CD138 staining and diagnosed without chronic endometritis according to the published criteria<sup>70</sup>.

### Tissue dissociation for single-cell transcriptomic sequencing

A one-step dissociation protocol was used to disperse fresh endometrial tissue<sup>71</sup>. Before dissociation, the tissue was rinsed with cold phosphate-buffered saline (PBS, Gibco) on a Petri dish to remove blood and mucus, and minced into small pieces using the surgical blade in 500 µl of DMEM-F12 (Gibco) supplemented with 1% fetal bovine serum albumin (ThermoFisher), 1% penicillin-streptomycin (Gibco) and 1% glutamine (Gibco). Tissue digestion was then immediately performed using DMEM-F12 (Gibco) medium containing DNase I (4 mg/ml, Worthington) and collagenase III (2.5 mg/ml, Worthington) in a 50-ml Falcon tube, which was horizontally incubated in a water bath at 37 °C with constant shaking for 1 h. After digestion, the cell suspension was filtered through 40 µm sieves (BD Bioscience) and loaded onto Ficoll-Paque (GE Healthcare) density gradient for red blood cell removal. Further removal of red blood cells was conducted using the red blood lysis solution (Miltenyi) for 5 min at room temperature. Dead cells were removed using the MACS dead cell removal kit (Miltenyi) following the manufacturer's protocol. Cell viability and concentration of the resulting single-cell suspension were assessed by a Countess™3 Automated Cell Counter (Life) for subsequent scRNA-seq experiments. To minimize operation variation, tissue processing and dissociation was performed by the same technician (J.W.).

### Single-cell capture, library preparation, and sequencing

The qualified endometrial single-cell suspensions with at least 80% cell viability and more than 20,000 cells were placed in a cold box at 4 °C, and an appropriate number of cells were loaded onto a Chromium Controller platform within 2 h. Single-cell encapsulation, barcoding, reverse transcription, cDNA generation, and library construction were performed following the manufacturer's protocol (Single Cell 3' reagent kit v3.1, 10X Genomics). Single-cell libraries of each donor were sequenced with a pair-end mode (150 bp) on a DNBSEQ-T7 instrument (GenePlus Technology) with a minimum sequencing depth of 50,000 reads/ per cell.

### Single-cell data pre-processing, quality control, and clustering

For each sample, the raw sequencing data was separately processed by the Cell Ranger pipeline (v.7.0.0) with default parameters for alignment and cell recovery using the GRCh38 reference genome. The filtered barcode matrices were loaded into the R package Seurat (v.4.1.1) to generate the cell-by-gene matrix<sup>72</sup>. Cells with less than 200 genes, or more than 25% mitochondrial reads were filtered out. Doublet cells were further filtered out for each sample using the R package DoubletFinder (v.2.0.3)<sup>73</sup>. Samples were then concatenated and integrated using the Seurat package. Genes expressed in less than 10 cells in the concatenated matrix were filtered out. The top 3000 highly variable genes (HVGs) were selected for dimensional reduction using principal component analysis. The first 50 principal components were used for batch effect removal by the method harmony (v.0.1.1)<sup>74</sup> which is packaged in the SeuratWrappers (v.0.3.1). The first 20 reduced dimensions of harmony were used for subsequent clustering by the Shared Nearest Neighbor (SNN) modularity optimization-based method and visualization by the Uniform Manifold Approximation and Projection (UMAP) method. Small clusters (less than 100 cells) with exceptional high UMI count, detected genes and percentage of mitochondrial reads were removed. Repeated analysis was performed until no aforementioned such cluster were present. Similar filtering and clustering processes were applied to specific cell subtype analyses.

### Differential expression analysis

Differentially expressed genes (DEGs) were identified using two approaches. With the function 'FindMarkers' in the Seurat package, DEGs were identified as log<sub>2</sub>fc.threshold >1 and adjusted *p* value < 0.05 using the method MAST which was developed specifically for single-cell data<sup>75</sup>. Meanwhile, the R package Cerepo (v.1.6.0) was also used to identify DEGs with *p*-value < 0.05 which was effective in the identification of cell identity genes<sup>76</sup>.

### Functional enrichment analysis

Functional enrichment analysis was performed both for cluster annotation and biological investigation and interpretation. Briefly, the defined gene set was subjected to Enrichr (<https://maayanlab.cloud/Enrichr/>) analysis<sup>77</sup>. Results from databases 'Reactome 2022', 'KEGG 2021', and 'MSigDB Hallmark 2020' were included. Terms with adjusted *p*-value < 0.05 were considered significant.

### Single-cell data annotation

Major endometrial cell types were manually annotated based on the expression of canonical markers collected from literature<sup>4,18–22,25,71</sup>. For annotation of typical cell type sub-clustering, high-resolution clusters were first identified. Canonical marker expression, cluster-specific gene identification as well as corresponding functional enrichment, and cluster tree construction with the R package clustree (0.5.0) were performed. Adjacent clusters on the UMAP with similar properties were combined to form a final cluster.

### Module score analysis

The 'AddModuleScore' function in the Seurat package was used to determine a senescence score for non-immune cells and an inflammation score for stromal cells and immune cells based on the expression of a validated senescence gene set SenMayo<sup>39</sup> and the gene set of HALLMARK\_INFLAMMATORY\_RESPONSE from MSigDB<sup>42</sup>, respectively. The validation of SenMayo gene set to indicate endometrium ageing was conducted utilizing identified human endometrial ageing genes<sup>40</sup> through intersection enrichment analysis (hypergeometric test), as well as gene expression enrichment analysis (GSVA) in both normal and senescent endometrial stromal cells using the bulk RNA-seq dataset<sup>78</sup>.

### Deconvolution analysis

We collected bulk RNA-seq data on human endometrium from the Gene Expression Omnibus database. The data inclusion criteria were: 1. RNA-seq was performed on the endometrium of women with normal menstrual cycles and without gynecological diseases. 2. The sampling time of each patient was meticulously recorded in detail and the form of LH+n. We downloaded the raw count data from different studies (GSE106602, GSE185392, GSE98386) and integrated them. The batch effect was corrected using the ComBat function in the R package sva (v.3.42.0). The data was then converted to transcript per million (TPM). Of the 81 included samples, the cellular composition was determined by deconvolution analysis with the R package DeconRNASeq (v.1.36.0) referencing the gene expression matrices of the major cell types identified in this study. Boxplots were used to visualize the proportions of each major cell type in the samples.

### RNA velocity analysis

The software Velocity (v.0.17.17)<sup>79</sup> was employed to compute the counts of spliced and unspliced mRNA within the single-cell sequencing data of each sample, resulting in a count matrix representing the mRNA splicing status. To analyze the developmental trajectory of endometrial epithelial cell subtypes, the Python package scVelo (v.0.2.5)<sup>80</sup> was used for data preprocessing, and RNA velocity and transcription rates were modeled using the Python package UniTelo



(v.0.1.6)<sup>81</sup> with 2,000 HVGs. A unified latent time across the whole transcriptome was also calculated using UniTelo.

### Location of cell types in spatial transcriptome data

The spatial transcriptomic dataset of human endometrium (Visium) was obtained from ArrayExpress with the accession number E-MTAB-9260<sup>19</sup>. To identify the putative spatial locations of the epithelial subpopulations defined in the present scRNA-seq study, the Python package Cell2Location (v.0.1.3)<sup>82</sup> was used to decompose the spatial spots into epithelial cell-subtype abundance estimates based on the cell-subtype expression signatures.

### Variational autoencoder (VAE) modeling of time inference and prediction at single-cell level

A VAE model based on the probabilistic latent space was constructed to infer the luteal time of cells taking into consideration prior time information. Structurally, this model consists of an encoder, a cell-decoder, and a time-decoder (Fig. 2a). The encoder encodes the pre-processed cell-by-gene expression matrix with a luteal time label (LH +n) to a low-dimensional distribution. The cell decoder reconstructs the input expression data from latent space using a generative model, while the time decoder extracts the time information using a supervised regression model. The detailed preprocessing step and modeling process and parameters are shown in Supplementary Note.

### Psupertime analysis

Based on the normalized gene expression matrix and the HVGs identified in Seurat (v.4.3.0), coefficients of HVGs were determined and genes with non-zero coefficients were used to project cells onto a pseudo time axis with prior sampling time information using the R package psupertime (v.0.2.6)<sup>32</sup>. Pseudotime distribution was then visualized for different cell types.

### Time-associated gene identification

Time-association (TA) of a gene was calculated using two methods. In the first method, the identification of TA genes for discrete groups was performed using the R package variancePartition (1.30.0)<sup>30</sup> for each cell type/subtype. Discrete-time was firstly transformed to  $[-1,1]$  as a continuous variable by subtracting 7 and dividing by 4. Variance explained by time was calculated when decomposing the variance of each gene into a transformed time as a fixed effect, the donor label as a random effect, and the residual. Variance greater than 0.1 was considered as TA genes. In the second method relying on the reconstructed luteal time, identification of TA genes was performed by calculating the mutual information (MI) score between the expression and the predicted time using the Java implementation method as introduced by an independent study<sup>18</sup>. A MI score greater than 0.1 was considered as a TA gene for a specific cell type.

### Time-associated gene ordering and clustering

To estimate the predicted luteal time at which a gene reached maximum expression, normalized expression of genes was firstly denoised and standardized as Z-score. Cells were ordered by sampling group and the predicted luteal time within each group. Based on the cell ordering, genes were then sorted according to the position of cells with top expression:

$$X, \left( X = \max \left\{ \text{ceiling} \left( \frac{n}{300} \right), 10 \right\} \right) \quad (1)$$

Clustering of genes was performed with the “hclust” package in R 4.1.2 ( $k=5$ ), and the order of the clusters was determined by the weight of the position in the cell order of groups.

### Single-cell and spatial ligand-receptor interaction analysis

Cell-cell interactions between different cell lineages were inferred by the R package CellChat (v.1.6.1) based on ligand-receptor pairs<sup>83</sup>. Specific expression of a receptor by one cell type and a corresponding ligand by another cell type was identified to reflect potential interaction between the cell types. The average expression values of the individual ligand-receptor complex in the corresponding interacting pairs of cell types were calculated to measure the interaction strength. The enriched ligand-receptor interactions between two cell subsets were calculated based on the permutation test. Significant ligand-receptor pairs were identified with  $P$ -value  $< 0.05$ .

To identify significant spatially co-expressed ligand-receptor pairs for endometrium, spatial transcriptome data of human endometrium deposited in ArrayExpress with the accession number E-MTAB-9260 was utilized<sup>19</sup>. With the public dataset, the Python package SpatialDM (v.0.1.0) was employed for ligand-receptor co-expression, local spots interaction, and communication pattern analysis<sup>84</sup>. A  $P$  value  $< 0.05$  was considered as significant.

### Protein-protein network analysis

Protein-protein interactions (PPIs) of the interested gene set were screened using the STRING database (<https://string-db.org/>, version: 12.0), with the confidence threshold value  $\geq 0.4$  (medium confidence) and false discovery rate stringency 5% (medium).

### Immunofluorescence

Formalin-fixed paraffin-embedded endometrial tissue slides (5  $\mu\text{m}$ ) were deparaffinized through incubation in xylene twice for 5 min each. Next, the slides were dehydrated in a series of ethanol gradients (2 $\times$  pure ethanol, followed by 1 $\times$  95% ethanol, 1 $\times$  85% ethanol, and 1 $\times$  75% ethanol for 4 min each). After washing with distilled water, antigen retrieval was performed by incubating the slides in sodium citrate antigen retrieval buffer (pH 6.0) in a microwave oven with high mode for 5 min and low mode for 15 min. After cooling down, the slides were washed with PBS for 5 min. A hydrophobic barrier was then drawn around the tissue sections with a PAP pen. To reduce non-specific binding, the sections were blocked in a blocking buffer containing 5% BSA/0.2% Triton-X100 at room temperature for 1 h. Next, the slides were incubated with diluted primary antibodies against EPCAM (1:200 dilutions, #AF960, R&D Systems), CDH1 (1:200 dilutions, #20874-1-AP, proteintech), EDG7 (1:100 dilutions, #19509-1-AP, proteintech), FOXA2 (1:300, #ab108422, Abcam), LGR5 (1:100 dilutions, # PA5-23000, Invitrogen), VIM (1:100 dilutions, #ab16700, Abcam), SPP1 (1:100 dilutions, #ab214050, Abcam), CD44 (1:100 dilutions, #ab316123, Abcam), CD45 (1:100 dilutions, #14-0459-82, Invitrogen), or c-Jun (1:100 dilutions, #ab40766, Abcam) overnight at 4 °C. Following three washes in PBS-T for 10 min each, the tissue slides were incubated in appropriate diluted secondary antibodies, including Alexa Fluor 568 goat anti-mouse antibody (1:400 dilutions, #ab175473, Abcam) or Alexa Fluor 647 goat anti-rabbit antibody (1:400 dilutions, ab150099, Abcam) at room temperature for 1 h in the dark. After washing three times in PBS-T for 10 min each, the slides were mounted with antifade mounting medium and DAPI (P0131, Beyotime). Confocal fluorescence images of the sections were captured using a ZEISS Axio-Imager\_LSM-900 laser scanning confocal microscope.

### RNA extraction, cDNA synthesis, and quantitative real-time polymerase chain reaction

Total RNA was extracted using the FastPure Cell/Tissue Total RNA Isolation Kit V2 (Vazyme) according to the manufacturer's protocol. The final RNA concentration was measured by a Nanodrop 2000 (Thermo). Reverse transcription was performed using the HiScript III All-in-one RT SuperMix Perfect for qPCR (Vazyme) following the standard protocol. Quantitative polymerase chain reaction (qPCR) was performed using the Taq Pro Universal SYBR qPCR Master Mix

(Vazyme) in a 7500 Real-Time PCR system (Applied Biosystems). Gene expression was normalized to GAPDH. Primers used were as follows:

**CDHI:** F-TCTGCTGCTCTTGCTGTTTCTTC, R-TCTCCGCTCCTTC TTCATCATAG;

**MTIX:** F-GACCCCAACTGCTCCTGCTC, R-ACACTTGGCACAGCCC ACAG;

**IFNG:** F-AGAGTGTGGAGACCATCAAGGAAG, R-TGCGTTGGACAT TCAAGTCAGTTAC.

### Statistics & reproducibility

No statistical method was used to predetermine sample size. No data were excluded from the analysis. The recruited donors were randomized into different time points for sample collection. The investigators were not blind to allocation during experiments and outcome assessment.

### Reporting summary

Further information on research design is available in the Nature Portfolio Reporting Summary linked to this article.

### Data availability

The processed sequencing data generated in this study have been deposited in the NCBI's Gene Expression Omnibus (GEO) under accession code [GSE250130](#). The raw sequencing data generated in this study have been deposited in the Sequence Read Archive under accession code [PRJNA1051672](#). Public datasets used in this study: bulk transcriptomic datasets of human endometrium for deconvolution study deposited in GEO under the accession codes [GSE106602](#), [GSE185392](#), and [GSE98386](#); bulk transcriptomic dataset of human endometrial stromal cells for GSVA analysis deposited in GEO under the accession code [GSE160702](#); single-cell transcriptomic dataset of human endometrium generated by Smart-seq and 10X genomics deposited in GEO under accession code [GSE111976](#); single-cell transcriptomic datasets of RIF endometrium deposited in GEO database under accession codes [GSE183837](#) and [GSE223672](#); and the spatial transcriptomic dataset generated by Visium deposited in ArrayExpress under the accession code [E-MTAB-9260](#). Source data are provided with this paper.

### Code availability

The newly developed computational method StemVAE<sup>85</sup> is freely available as a Python package on GitHub ([https://github.com/awa121/stemVAE\\_endometrium](https://github.com/awa121/stemVAE_endometrium)). Other specific codes relating to this study are accessible, with no restrictions, upon request to D.C. (caodd@hku-szh.org).

### References

- Noyes, R. W., Hertig, A. T. & Rock, J. Dating the endometrial biopsy. *Am. J. Obstet. Gynecol.* **122**, 262–263 (1975).
- Wilcox, A. J., Baird, D. D. & Weinberg, C. R. Time of implantation of the conceptus and loss of pregnancy. *N. Engl. J. Med.* **340**, 1796–1799 (1999).
- Croxatto, H. B. et al. Studies on the duration of egg transport by the human oviduct. II. Ovum location at various intervals following luteinizing hormone peak. *Am. J. Obstet. Gynecol.* **132**, 629–634 (1978).
- Achache, H. & Revel, A. Endometrial receptivity markers, the journey to successful embryo implantation. *Hum. Reprod. Update* **12**, 731–746 (2006).
- Brosens, J. J. et al. Uterine selection of human embryos at implantation. *Sci. Rep.* **4**, 3894 (2014).
- Muter, J., Lynch, V. J., McCoy, R. C. & Brosens, J. J. Human embryo implantation. *Development* **150**, <https://doi.org/10.1242/dev.201507> (2023).
- Berkhout, R. P. et al. High-quality human preimplantation embryos stimulate endometrial stromal cell migration via secretion of microRNA hsa-miR-320a. *Hum. Reprod.* **35**, 1797–1807 (2020).
- Shmygol, A. & Brosens, J. J. Proteinase Activated Receptors Mediate the Trypsin-Induced Ca(2+) Signaling in Human Uterine Epithelial Cells. *Front. Cell Dev. Biol.* **9**, 709902 (2021).
- Kong, C. S. et al. Embryo biosensing by uterine natural killer cells determines endometrial fate decisions at implantation. *FASEB J.* **35**, e21336 (2021).
- Brosens, J. J. et al. Maternal selection of human embryos in early gestation: Insights from recurrent miscarriage. *Semin. Cell Dev. Biol.* **131**, 14–24 (2022).
- Ruane, P. T. et al. Trophectoderm differentiation to invasive syncytiotrophoblast is promoted by endometrial epithelial cells during human embryo implantation. *Hum. Reprod.* **37**, 777–792 (2022).
- Liu, D. et al. Primary specification of blastocyst trophectoderm by scRNA-seq: New insights into embryo implantation. *Sci. Adv.* **8**, eabj3725 (2022).
- Liu, W. M. et al. Let-7 derived from endometrial extracellular vesicles is an important inducer of embryonic diapause in mice. *Sci. Adv.* **6**, eaaz7070 (2020).
- Sehring, J., Beltsos, A. & Jeelani, R. Human implantation: The complex interplay between endometrial receptivity, inflammation, and the microbiome. *Placenta* **117**, 179–186 (2022).
- Coughlan, C. et al. Recurrent implantation failure: definition and management. *Reprod. Biomed. Online* **28**, 14–38 (2014).
- Franasiak, J. M. et al. A review of the pathophysiology of recurrent implantation failure. *Fertil. Steril.* **116**, 1436–1448 (2021).
- Sebastian-Leon, P., Garrido, N., Remohi, J., Pellicer, A. & Diaz-Gimeno, P. Asynchronous and pathological windows of implantation: two causes of recurrent implantation failure. *Hum. Reprod.* **33**, 626–635 (2018).
- Wang, W. et al. Single-cell transcriptomic atlas of the human endometrium during the menstrual cycle. *Nat. Med.* **26**, 1644–1653 (2020).
- Garcia-Alonso, L. et al. Mapping the temporal and spatial dynamics of the human endometrium in vivo and in vitro. *Nat. Genet.* **53**, 1698–1711 (2021).
- Tan, Y. et al. Single-cell analysis of endometriosis reveals a coordinated transcriptional programme driving immunotolerance and angiogenesis across eutopic and ectopic tissues. *Nat. Cell Biol.* **24**, 1306–1318 (2022).
- Fonseca, M. A. S. et al. Single-cell transcriptomic analysis of endometriosis. *Nat. Genet.* **55**, 255–267 (2023).
- Lv, H. et al. Deciphering the endometrial niche of human thin endometrium at single-cell resolution. *Proc. Natl Acad. Sci. USA* **119**, <https://doi.org/10.1073/pnas.2115912119> (2022).
- Santamaria, X. et al. Decoding the endometrial niche of Asherman's Syndrome at single-cell resolution. *Nat. Commun.* **14**, 5890 (2023).
- Lucas, E. S. et al. Recurrent pregnancy loss is associated with a pro-senescent decidual response during the peri-implantation window. *Commun. Biol.* **3**, 37 (2020).
- Lai, Z. Z. et al. Single-cell transcriptome profiling of the human endometrium of patients with recurrent implantation failure. *Theranostics* **12**, 6527–6547 (2022).
- Xu, Q. X., Zhang, W. Q., Lu, L., Wang, K. Z. & Su, R. W. Distinguish Characters of Luminal and Glandular Epithelium from Mouse Uterus Using a Novel Enzyme-Based Separation Method. *Reprod. Sci.* **30**, 1867–1877 (2023).
- Tempest, N., Baker, A. M., Wright, N. A. & Hapangama, D. K. Does human endometrial LGR5 gene expression suggest the existence of another hormonally regulated epithelial stem cell niche? *Hum. Reprod.* **33**, 1052–1062 (2018).

28. Molotkov, A., Mazot, P., Brewer, J. R., Cinalli, R. M. & Soriano, P. Distinct Requirements for FGFR1 and FGFR2 in Primitive Endoderm Development and Exit from Pluripotency. *Dev. Cell* **41**, 511–526 e514 (2017).
29. Tempest, N. et al. Novel microarchitecture of human endometrial glands: implications in endometrial regeneration and pathologies. *Hum. Reprod. Update* **28**, 153–171 (2022).
30. Hoffman, G. E. & Schadt, E. E. variancePartition: interpreting drivers of variation in complex gene expression studies. *BMC Bioinforma.* **17**, 483 (2016).
31. Lipecki, J. et al. EndoTime: non-categorical timing estimates for luteal endometrium. *Hum. Reprod.* **37**, 747–761 (2022).
32. Macnair, W., Gupta, R. & Claassen, M. psuptime: supervised pseudotime analysis for time-series single-cell RNA-seq data. *Bioinformatics* **38**, i290–i298 (2022).
33. Horcujadas, J. A. et al. Controlled ovarian stimulation induces a functional genomic delay of the endometrium with potential clinical implications. *J. Clin. Endocrinol. Metab.* **93**, 4500–4510 (2008).
34. Ng, S. W. et al. Endometrial Decidualization: The Primary Driver of Pregnancy Health. *Int. J. Mol. Sci.* **21**, <https://doi.org/10.3390/ijms21114092> (2020).
35. Brighton, P. J. et al. Clearance of senescent decidual cells by uterine natural killer cells in cycling human endometrium. *Elife* **6**, <https://doi.org/10.7554/eLife.31274> (2017).
36. Evans, J. et al. Fertile ground: human endometrial programming and lessons in health and disease. *Nat. Rev. Endocrinol.* **12**, 654–667 (2016).
37. Salamonsen, L. A., Hutchison, J. C. & Gargett, C. E. Cyclical endometrial repair and regeneration. *Development* **148**, <https://doi.org/10.1242/dev.199577> (2021).
38. Jaschke, N. P. et al. Dickkopf1 fuels inflammatory cytokine responses. *Commun. Biol.* **5**, 1391 (2022).
39. Saul, D. et al. A new gene set identifies senescent cells and predicts senescence-associated pathways across tissues. *Nat. Commun.* **13**, 4827 (2022).
40. Devesa-Peiro, A., Sebastian-Leon, P., Parraga-Leo, A., Pellicer, A. & Diaz-Gimeno, P. Breaking the ageing paradigm in endometrium: endometrial gene expression related to cilia and ageing hallmarks in women over 35 years. *Hum. Reprod.* **37**, 762–776 (2022).
41. Winkler, I. et al. The cycling and aging mouse female reproductive tract at single-cell resolution. *Cell* **187**, 981–998 e925 (2024).
42. Liberzon, A. et al. The Molecular Signatures Database (MSigDB) hallmark gene set collection. *Cell Syst.* **1**, 417–425 (2015).
43. Adiguzel, D. & Celik-Ozenci, C. FoxO1 is a cell-specific core transcription factor for endometrial remodeling and homeostasis during menstrual cycle and early pregnancy. *Hum. Reprod. Update* **27**, 570–583 (2021).
44. Li, R. et al. The role of epithelial progesterone receptor isoforms in embryo implantation. *iScience* **24**, 103487 (2021).
45. Plaisier, C. L. et al. Causal Mechanistic Regulatory Network for Glioblastoma Deciphered Using Systems Genetics Network Analysis. *Cell Syst.* **3**, 172–186 (2016).
46. Vasquez, Y. M. et al. FOXO1 regulates uterine epithelial integrity and progesterone receptor expression critical for embryo implantation. *PLoS Genet* **14**, e1007787 (2018).
47. Reardon, S. N. et al. CDH1 is essential for endometrial differentiation, gland development, and adult function in the mouse uterus. *Biol. Reprod.* **86**, 141–110 (2012). 141.
48. Bi, Y. et al. HOXA10 improves endometrial receptivity by upregulating E-cadherin. *Biol. Reprod.* **106**, 992–999 (2022).
49. Berneau, S. C. et al. Investigating the role of CD44 and hyaluronate in embryo-epithelial interaction using an in vitro model. *Mol. Hum. Reprod.* **25**, 265–273 (2019).
50. Hu, S. et al. Transcriptomic changes during the pre-receptive to receptive transition in human endometrium detected by RNA-Seq. *J. Clin. Endocrinol. Metab.* **99**, E2744–2753, (2014).
51. Ruiz-Alonso, M. et al. The endometrial receptivity array for diagnosis and personalized embryo transfer as a treatment for patients with repeated implantation failure. *Fertil. Steril.* **100**, 818–824 (2013).
52. He, A. et al. The role of transcriptomic biomarkers of endometrial receptivity in personalized embryo transfer for patients with repeated implantation failure. *J. Transl. Med.* **19**, 176 (2021).
53. Diaz-Gimeno, P. et al. The accuracy and reproducibility of the endometrial receptivity array is superior to histology as a diagnostic method for endometrial receptivity. *Fertil. Steril.* **99**, 508–517 (2013).
54. Chen, D., Xu, Q., Mao, X., Zhang, J. & Wu, L. Reproductive history does not compromise subsequent live birth and perinatal outcome following in-vitro fertilization: analysis of 25 329 first frozen-thawed embryo transfer cycles without preimplantation genetic testing for aneuploidy. *Ultrasound Obstet. Gynecol.* **62**, 430–438 (2023).
55. Qiu, J. et al. Impact of recurrent pregnancy loss history on reproductive outcomes in women undergoing fertility treatment. *Am. J. Obstet. Gynecol.* **228**, 66 e61–66 e69 (2023).
56. Failure, E. W. Go. R. I. et al. ESHRE good practice recommendations on recurrent implantation failure. *Hum. Reprod. Open* **2023**, hoad023 (2023).
57. Donoghue, J. F. et al. Endometrial uNK cell counts do not predict successful implantation in an IVF population. *Hum. Reprod.* **34**, 2456–2466 (2019).
58. Chen, X. et al. Measurement of uterine natural killer cell percentage in the periimplantation endometrium from fertile women and women with recurrent reproductive failure: establishment of a reference range. *Am. J. Obstet. Gynecol.* **217**, 680 e681–680 e686 (2017).
59. Victorelli, S. et al. Apoptotic stress causes mtDNA release during senescence and drives the SASP. *Nature* **622**, 627–636 (2023).
60. Ruan, Y. C., Chen, H. & Chan, H. C. Ion channels in the endometrium: regulation of endometrial receptivity and embryo implantation. *Hum. Reprod. Update* **20**, 517–529 (2014).
61. Diao, H. L. et al. Effects of androgen on embryo implantation in the mouse delayed-implantation model. *Fertil. Steril.* **90**, 1376–1383 (2008).
62. Owusu-Akyaw, A., Krishnamoorthy, K., Goldsmith, L. T. & Morelli, S. S. The role of mesenchymal-epithelial transition in endometrial function. *Hum. Reprod. Update* **25**, 114–133 (2019).
63. Saxtorph, M. H. et al. Assessing endometrial receptivity after recurrent implantation failure: a prospective controlled cohort study. *Reprod. Biomed. Online* **41**, 998–1006 (2020).
64. King, A. E. & Critchley, H. O. Oestrogen and progesterone regulation of inflammatory processes in the human endometrium. *J. Steroid Biochem Mol. Biol.* **120**, 116–126 (2010).
65. Chi, R. A. et al. Human Endometrial Transcriptome and Progesterone Receptor Cistrome Reveal Important Pathways and Epithelial Regulators. *J. Clin. Endocrinol. Metab.* **105**, e1419–1439, (2020).
66. Mazur, E. C. et al. Progesterone receptor transcriptome and cistrome in decidualized human endometrial stromal cells. *Endocrinology* **156**, 2239–2253 (2015).
67. Amjadi, F. et al. The uterine immunological changes may be responsible for repeated implantation failure. *J. Reprod. Immunol.* **138**, 103080 (2020).
68. Liang, P. Y. et al. The pro-inflammatory and anti-inflammatory cytokine profile in peripheral blood of women with recurrent implantation failure. *Reprod. Biomed. Online* **31**, 823–826 (2015).
69. Cimadomo, D., Craciunas, L., Vermeulen, N., Vomstein, K. & Toth, B. Definition, diagnostic and therapeutic options in recurrent implantation failure: an international survey of clinicians and embryologists. *Hum. Reprod.* **36**, 305–317 (2021).
70. Liu, Y. et al. Comparison of the prevalence of chronic endometritis as determined by means of different diagnostic methods in women with and without reproductive failure. *Fertil. Steril.* **109**, 832–839 (2018).



71. Cao, D., Chan, R. W. S., Ng, E. H. Y., Gemzell-Danielsson, K. & Yeung, W. S. B. Single-cell RNA sequencing of cultured human endometrial CD140b(+)CD146(+) perivascular cells highlights the importance of in vivo microenvironment. *Stem Cell Res. Ther.* **12**, 306 (2021).
72. Hao, Y. et al. Integrated analysis of multimodal single-cell data. *Cell* **184**, 3573–3587 e3529 (2021).
73. McGinnis, C. S., Murrow, L. M. & Gartner, Z. J. DoubletFinder: Doublet Detection in Single-Cell RNA Sequencing Data Using Artificial Nearest Neighbors. *Cell Syst.* **8**, 329–337 e324 (2019).
74. Korsunsky, I. et al. Fast, sensitive and accurate integration of single-cell data with Harmony. *Nat. Methods* **16**, 1289–1296 (2019).
75. Finak, G. et al. MAST: a flexible statistical framework for assessing transcriptional changes and characterizing heterogeneity in single-cell RNA sequencing data. *Genome Biol.* **16**, 278 (2015).
76. Kim, H. J. et al. Uncovering cell identity through differential stability with Cepo. *Nat. Computational Sci.* **1**, 784–790 (2021).
77. Xie, Z. et al. Gene Set Knowledge Discovery with Enrichr. *Curr. Protoc.* **1**, e90 (2021).
78. Deryabin, P. I. & Borodkina, A. V. Stromal cell senescence contributes to impaired endometrial decidualization and defective interaction with trophoblast cells. *Hum. Reprod.* **37**, 1505–1524 (2022).
79. La Manno, G. et al. RNA velocity of single cells. *Nature* **560**, 494–498 (2018).
80. Bergen, V., Lange, M., Peidli, S., Wolf, F. A. & Theis, F. J. Generalizing RNA velocity to transient cell states through dynamical modeling. *Nat. Biotechnol.* **38**, 1408–1414 (2020).
81. Gao, M., Qiao, C. & Huang, Y. UniTelo: temporally unified RNA velocity reinforces single-cell trajectory inference. *Nat. Commun.* **13**, 6586 (2022).
82. Kleshchevnikov, V. et al. Cell2location maps fine-grained cell types in spatial transcriptomics. *Nat. Biotechnol.* **40**, 661–671 (2022).
83. Jin, S. et al. Inference and analysis of cell-cell communication using CellChat. *Nat. Commun.* **12**, 1088 (2021).
84. Li, Z., Wang, T., Liu, P. & Huang, Y. SpatialDM for rapid identification of spatially co-expressed ligand-receptor and revealing cell-cell communication patterns. *Nat. Commun.* **14**, 3995 (2023).
85. Liu, Y., Cao, D. & Huang, Y. stemVAE\_endometrium. *Zenodo*, <https://zenodo.org/records/13950075> (2024).

## Acknowledgements

The authors thank Geneplus-Shenzhen for its sequencing expertise, Pathologist Feifei Luo for her advice in endometrial histology, and Mr. Qunxiong Zeng for his support in immune-related discussion and flow cytometry analysis during revision. This study was jointly supported by the Shenzhen Fundamental Research Program of China (No. JCYJ20220818103013028, to Y.Y.), National Key Research and Development Program of China (No. 2022YFC2702500, No.2022YFC2702503, to Y.Y.), the National Natural Science Foundation of China (No. 62222217, to Y.H.), High Level-Hospital Program, Health Commission of Guangdong Province, China (No. HKUSZH202207001 to Y.Y.), the University of Hong Kong through a startup fund and a seed fund (to Y.H.), the Guangdong Basic and Applied Basic Research Foundation, China (No. 2023A1515220177, to D.C.), and Shenzhen Science

and Technology Program (KQTD20190929172749226 to Y.Y. and W.S.B.Y.). The graphics in Figs. 1a, 5c, f (partial) were created with BioRender (<https://www.biorender.com/>).

## Author contributions

D.C., W.S.B.Y., Y.H., and Y.Y. designed the study. Y.F.C., Y.S., and Y.Y. recruited the donors, and collected the endometrial biopsy samples and clinical information. J.W., B.Z., Y.Z., and Y.L.L. processed the samples and performed the experiments. Y.J.L. and Y.H. developed StemVAE with input from D.C., D.C., Y.J.L., K.Z., B.Z., Y.L., X.X. analyzed the data with input from Y.H. and Y.C., D.C., W.S.B.Y., Y.H. and Y.Y. interpreted the results. D.C. and Y.J.L. wrote the manuscript with input from all authors.

## Competing interests

X.X. was an employee of Geneplus-Shenzhen. All the other authors declare no competing interests.

## Additional information

**Supplementary information** The online version contains supplementary material available at <https://doi.org/10.1038/s41467-024-55419-z>.

**Correspondence** and requests for materials should be addressed to William Shu Biu Yeung, Yuanhua Huang or Yuanqing Yao.

**Peer review information** *Nature Communications* thanks Nardhy Gomez-Lopez, and the other, anonymous, reviewers for their contribution to the peer review of this work. A peer review file is available.

**Reprints and permissions information** is available at <http://www.nature.com/reprints>

**Publisher's note** Springer Nature remains neutral with regard to jurisdictional claims in published maps and institutional affiliations.

**Open Access** This article is licensed under a Creative Commons Attribution-NonCommercial-NoDerivatives 4.0 International License, which permits any non-commercial use, sharing, distribution and reproduction in any medium or format, as long as you give appropriate credit to the original author(s) and the source, provide a link to the Creative Commons licence, and indicate if you modified the licensed material. You do not have permission under this licence to share adapted material derived from this article or parts of it. The images or other third party material in this article are included in the article's Creative Commons licence, unless indicated otherwise in a credit line to the material. If material is not included in the article's Creative Commons licence and your intended use is not permitted by statutory regulation or exceeds the permitted use, you will need to obtain permission directly from the copyright holder. To view a copy of this licence, visit <http://creativecommons.org/licenses/by-nc-nd/4.0/>.

© The Author(s) 2024

<sup>1</sup>Shenzhen Key Laboratory of Fertility Regulation, Reproductive Medicine Center, the University of Hong Kong-Shenzhen Hospital, Shenzhen, China. <sup>2</sup>School of Biomedical Sciences, the University of Hong Kong, Hong Kong SAR, China. <sup>3</sup>School of Artificial Intelligence, Jilin University, Jilin, China. <sup>4</sup>School of Medicine, Nankai University, Tianjin, China. <sup>5</sup>Genomics Institute, Geneplus-Shenzhen, Shenzhen, China. <sup>6</sup>Department of Obstetrics and Gynaecology, the University of Hong Kong, Hong Kong SAR, China. <sup>7</sup>Centre for Translational Stem Cell Biology, Building 17 W, The Hong Kong Science and Technology Park, Hong Kong SAR, China. <sup>8</sup>Department of Statistics and Actuarial Science, the University of Hong Kong, Hong Kong SAR, China. <sup>9</sup>Department of Gynecology and Obstetrics, Chinese PLA General Hospital, Beijing, China. <sup>10</sup>These authors contributed equally: Dandan Cao, Yijun Liu, Yanfei Cheng

✉ e-mail: [wsbyeung@hku.hk](mailto:wsbyeung@hku.hk); [yuanhua@hku.hk](mailto:yuanhua@hku.hk); [yaoyq\\_hkusz@126.com](mailto:yaoyq_hkusz@126.com)